ELECTRICAL OUTPUT EVALUATION OF A CONCENTRATED PHOTOVOLTAIC SYSTEM COUPLED WITH A PHASE CHANGE MATERIAL FOR QATAR WEATHER CONDITIONS

A Thesis

by

AHMED EISA ELBASHEER ABBAS

Submitted to the Office of Graduate and Professional Studies of
Texas A&M University
in partial fulfillment of the requirements for the degree of

MASTER OF SCIENCE

Chair of Committee,	Konstantinos E. Kakosimos
Committee Members,	Mohamed Nounou
	Hazem Nounou
Head of Department,	M. Nazmul Karim

December 2017

Major Subject: Chemical Engineering

ABSTRACT

Solar energy is a renewable energy resource and presents a ripe opportunity to meet international goals of reducing fossil fuel use and combating global warming. However solar energy has yet to make large market proliferation, accounting only for 1% of total electricity generation around the world. Concentrator Photovoltaics (CPV), which use concentrators to focus sunlight onto a smaller PV cell area, provide a way to increase electrical conversion efficiency while using less of the expensive PV cell material.

A disadvantage of using CPV systems is the increase in cell temperature due to concentration of sunlight, which leads to reduced electrical output. Phase change materials (PCM) can passively cool a CPV cell by absorbing heat through phase change, while maintaining a near constant temperature in the process, all while keeping the system relatively simple and modular. The objective of this thesis is the development of an integrated model that captures optical-electrical-thermal processes, to predict the power output and temperature profile of a Concentrator Photovoltaic-Phase Change Material (CPV-PCM) system. A case study using the model is made using Qatar weather conditions, to predict power output and temperature profile of a CPV-PCM system and compare with a flat-plate PV system. Results indicate the CPV-PCM system outperforming the PV system on power generation, although CPV system cell temperatures that are below PV system temperatures could only be achieved under 15x optical concentration ratio.

ACKNOWLEDGEMENTS

I would like to thank my committee chair, Dr. Konstantinos Kakosimos, and my committee members, Dr. Mohamed Nounou, and Dr. Hazem Nounou, for their support and valued feedback throughout this research. Special thanks go to Dr. Jawad Sarwar, for his invaluable help from the very start of this research effort, especially in providing the thermal-optical model used in this thesis.

I would also like to thank the Chemical Engineering department faculty and staff for their welcome and help during my studies, and thanks to my colleagues and friends for their support.

Finally, thanks to my mother, for her tireless help and support throughout this endeavor. This would not have happened without you. Thanks to my brothers for their constant encouragement. Thanks to my late father, who I am sure would have been proud of this achievement, may he rest in peace.

CONTRIBUTORS AND FUNDING SOURCES

This work was supervised by a thesis committee consisting of Dr. Konstantinos Kakosimos and Dr. Mohamed Nounou of the Department of Chemical Engineering and Dr. Hazem Nounou of the Department of Electrical Engineering.

The thermal-optical model, described in Section 3.2.2 was developed and provided by Dr. Jawad Sarwar.

All other work conducted for the thesis was completed by the student independently.

Graduate study was supported by a graduate assistantship from Texas A&M University at Qatar.

This work was made possible by a NPRP award [NPRP 7-674-2-252] from the Qatar National Research Fund (a member of The Qatar Foundation).

NOMENCLATURE

a	Ideality factor
A	Area (m^2)
B	B-operator
c	Heat capacity (kJ/kg.K)
c_e	Effective PCM heat capacity (kJ/kg.K)
c_l	Liquid PCM heat capacity (kJ/kg.K)
c_s	Solid PCM heat capacity (kJ/kg.K)
c-Si	Crystalline Silicon
C_g	Geometrical concentration ratio
CPV	Concentrator Photovoltaic
CPVPCM	Concentrator Photovoltaic – Phase change material
CR	Concentration ratio
DNI	Direct Normal Irradiance
e	Electron charge ($1.60217646 * 10^{-19}$ C)
E	Equation of time (h)
E_{gap}	Bandgap energy for silicon ($1.8 * 10^{-19}$ J)
F	View factor
FEM	Finite element method
G	Irradiance (W/m^2)
G_n	Nominal irradiance (1000 W/m^2)

GHI	Global Horizontal Irradiance
h	Width of system (m)
h_c	Convection heat transfer coefficient (W/m^2.K)
h_r	Radiation heat transfer coefficient (W/m^2.K)
H	Convection matrix
H	Heat loss by convection (W)
H_l	Local time
ΔH_g	Time lag due to longitude variation
ΔH_l	Time lag between given time zone and UTC
HCPV	High concentrator photovoltaic
I	Current (A)
I_{mp}	Current at maximum module power (A)
I_0	Reverse saturation current (A)
I_{pv}	Photocurrent (A)
I_{sc}	Short circuit current (A)
$I_{sc,n}$	Nominal short circuit current (A)
I-V	Current-Voltage
J	Jacobian matrix
J'	Rank of day after the first of January 2013
J_i	Jacobian matrix of boundary
J_u	Julian day of year
k	Conductivity (W/m.K)

k_B	Boltzmann constant (1.3806503 * 10^{-23} JK^{-1})
k_{ij}	Conductivity - i and j represent nodes (W/m.K)
K	Conductivity matrix
K	Extinction coefficient
K_I	Short circuit current temperature coefficient (%/K)
K_V	Open circuit voltage temperature coefficient (%/K)
l	Latitude (degrees)
LCPV	Low concentrator photovoltaic
M	Mass matrix
MCPV	Medium concentrator photovoltaic
MJ	Multi-junction
N	8-node Serendipity element
N_s	Number of cells in series
PCM	Phase change material
PDE	Partial differential equation
$P_{max,e}$	Experimental Maximum power (W)
$P_{max,m}$	Model predicted Maximum power (W)
PV	Photovoltaic
PVPCM	Photovoltaic – Phase change material
$\boldsymbol{q}$	Irradiance matrix
q	Irradiance after optical losses and electrical conversion (W/m^2)
q_{aol}	Irradiance after optical losses (W/m^2)

q_e	Irradiance after electrical conversion (W/m^2)
rf	Reflectance
$rf_{\parallel}$	Reflectance – parallel component
$rf_{\perp}$	Reflectance – perpendicular component
R	Radiation matrix
R	Heat loss by radiation (W)
R_p	Shunt resistance (Ω)
$R_{p,min}$	Minimum shunt resistance (Ω)
R_s	Series resistance (Ω)
$R_{s,n}$	Nominal series resistance (Ω)
s	PV inclination (degrees, radians)
sun	1 sun = 1000 W/m^2
STC	Standard Test Conditions (25 ℃, 1000 W/m^2)
t	Time (s)
T	Temperature (K)
ΔT	Temperature difference
$\dot{T}$	Time derivative of temperature (K/s)
T_1	PCM melting onset temperature (K)
T_2	PCM solidification endset temperature (K)
T_{amb}	Ambient temperature (K)
T_{sky}	Sky temperature (K)
T_{STC}	Temperature at standard test conditions (298 K)

v	Air velocity (m/s)
V	Voltage (V)
V_t	Thermal voltage (V)
V_{mp}	Voltage at maximum module power (V)
V_{oc}	Open-circuit voltage (V)
$V_{oc,n}$	Nominal open-circuit voltage (V)
x	Distance (m)
x_1	Component of X or distance in x-axis (m)
x_2	Component of X or distance in y-axis (m)
x_i	Distance in i direction (m)
x_j	Distance in j direction (m)
α	Absorptance
$\alpha_{\parallel}$	Absorptance – parallel component
$\alpha_{\perp}$	Absorptance – perpendicular component
δ	Sun declination angle (degrees, radians)
ε	Emissivity
η	Electrical efficiency (%)
η_O	Optical efficiency of concentrator (%)
θ_i	Incident angle (degrees, radians)
θ_t	Transmittance angle (degrees, radians)
μ	Power output temperature coefficient (%/K)
$\xi_{1,2}$	Natural coordinates

ρ	Density (kg/m^3)
σ	Stefan-Boltzmann constant ($5.67 * 10^{-8}$ $W/m^2.K^{-4}$)
τ	Transmittance
$\tau_{\parallel}$	Transmittance – parallel component
$\tau_{\perp}$	Transmittance – perpendicular component
τ_a	Transmittance coefficient after absorptance
φ	Azimuth angle (degrees, radians)
ω	Hour angle (degrees, radians)
Ω	Physical domain

TABLE OF CONTENTS

Page

LIST OF FIGURES

Page

LIST OF TABLES

Page

1. INTRODUCTION

1.1 Impetus for solar energy

Energy security and consumption have become an increasingly important part of today's economies and industries. As populations and industries continue to grow around the world, so too does their need for more energy, in forms of fuels or electricity. Non-renewable fossil fuels were, and still are an important part in meeting these energy demands, but it is well-documented that the increase in fossil fuel consumption, and subsequently the release of greenhouse gases, have led to global climate change, potentially leading to an increase in natural disasters around the world. In addition, fossil fuels, given their depletable nature, could not possibly last forever.

The Paris Agreement, signed on November 2016, and ratified, up to date, by 146 countries (UN 2016), aims to curb the pace of climate change by limiting global temperature rise to below 2 °C above pre-industrial levels. According to the International Energy Agency (IEA) in its World Energy Outlook 2016 (IEA 2016), renewable energy needs to account for 37% of power generation by 2040, up from 23% in 2016, to meet the Paris Agreement pledges. The IEA also points out that the pledges themselves would not be enough to curb CO_2 emissions to the 2 °C target, and would require tougher policies to fast-track low carbon technologies, including renewable energy.

Common sources of renewable energy include solar, wind, hydro and geothermal power. Solar power is a particularly lucrative venue, given the plentiful energy that could be harvested from the Sun. The two main technologies for harvesting solar power

are solar photovoltaic (PV), which converts incoming sunlight directly into electrical DC current, and solar thermal, which uses the thermal energy of sunlight for heating purposes, or to power steam turbines for electrical generation.

According to United Nations (UN) statistics collected up to 2014, solar energy only accounted for ~0.77% of the total electricity generation in the world (UN 2014), but in general, solar power adoption has seen exponential growth, rising from a mere 6.4 GW in 2006 to 227 GW in 2015 (IRENA 2016), and its share among the other renewable energy sources (of which hydro-power is the most dominant) is increasing, where in 2016 an additional 70 GW of solar power capacity was added, which represented a 32% growth from the previous year (IRENA 2017). It is clear then that the future for solar PV power is a promising one.

1.2 CPV systems and types of PV cells

Many technologies exist for solar PV, from the traditional and well established flat-plate PV panels, which use crystalline-silicon cells, to more novel approaches, such as Concentrator Photovoltaic (CPV) systems. CPV systems use optics (concentrators) to focus sunlight onto a PV cell, while using a tracking system, which mechanically orients the CPV panels towards the Sun. Tracking itself is not an exclusive feature of CPV, and can be applied to PV as well.

The degree of this concentration varies, from low (or LCPV, <10 suns), medium (MCPV, 10-100 suns) and high (HCPV, >100 suns). The term ‘sun’ here is used to refer to a standard condition, where one sun is equal to 1000 W/m^2. The key feature of CPV systems are the use of comparatively cheaper optics (made of glass/acrylic) to reduce the

amount of PV materials used (which account for 50% of PV system cost) (Amanlou, Hashjin et al. 2016), all while producing the same amount of power.

The general idea of the CPV system is shown in Figure 1. Instead of using more expensive PV material, the incoming sunlight is concentrated onto a smaller PV cell size, and because power generation directly depends on the intensity of sunlight, then the CPV system produces the same amount of power for less PV cell area. In fact, concentration actually increases the cell efficiency, so there is a double benefit to sunlight concentration in this regard (Gray 2011).

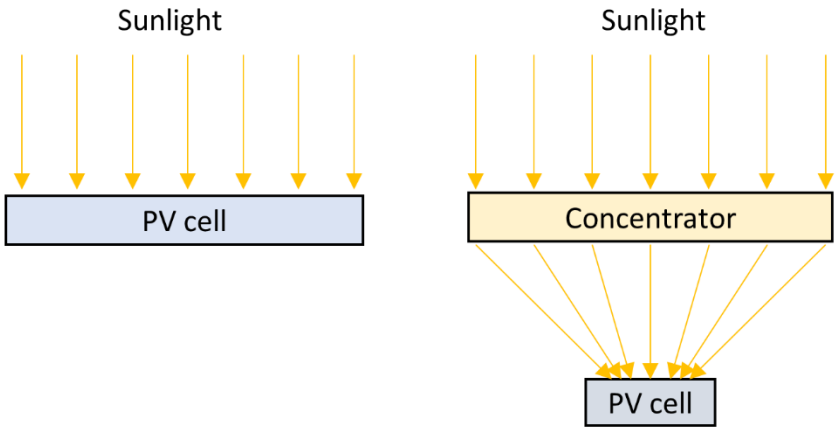

Figure 1: Simplified representation of a PV vs CPV system

Sunlight is mainly split into two components, the direct component, often called Direct Normal Irradiance (DNI), which accounts for 80% of the total irradiance on a clear day, and the diffuse component, which accounts for the other 20% (Luque and Andreev 2007). There is also the Global Horizontal Irradiance (GHI), which is the sum of direct and diffuse components for sunlight on a fixed horizontal facing surface.

CPV systems are especially useful in regions of the world with higher insolation, because the concentrator can only focus the DNI, which is more plentiful in areas without cloud coverage. Hence regions such as the Middle East are better suited for a CPV system (Fernández, Talavera et al. 2016).

There are various PV cell technologies, which include polycrystalline and monocrystalline silicon (collectively known as crystalline silicon or c-Si). They can also be called single-junction cells. This is based on the key mechanism of electricity generation in the PV cell, which happens in the p-n junction of the solar cell.

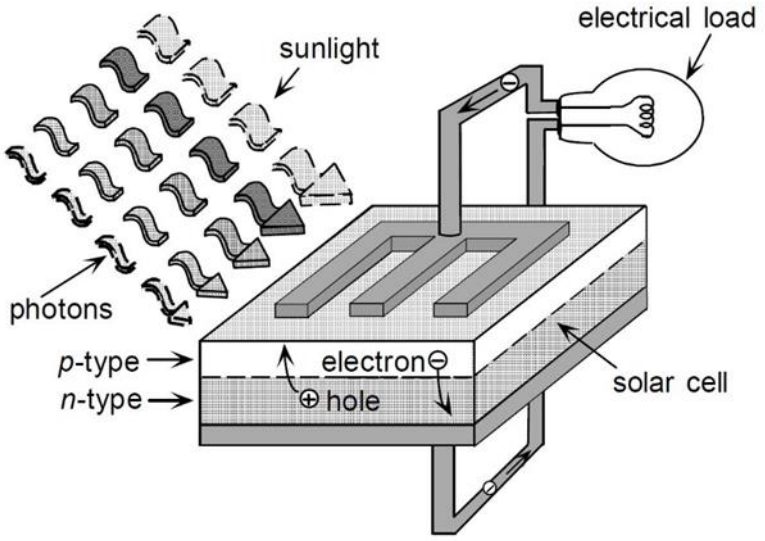

Figure 2: Single junction PV cell, reprinted from (Richards and Green 2006)

Figure 2 shows the operation of a PV cell. Photons of light strike the surface of a PV cell, where, depending on the bandgap of the material used, can lead to the creation of 'electron-hole pairs' which act as charge carriers. The band-gap can be thought of as the energy required by the photon to excite an electron within the PV material. The

electron is generated in the p-type material, which has an excess of free ‘holes’, and the hole is generated in the n-type material, which has an excess of free electrons. The electron and hole must cross the p-n junction to contribute to electricity generation, which does not always happen because they can recombine with their counterparts before crossing the junction. The energy that results from the recombination is generally lost as heat inside the PV cell (Richards and Green 2006).

The bandgap of a PV cell material is an important parameter because it determines the energy of photons that can generate an electrical current in the PV cell. Sunlight is a combination of waves at different wavelengths, and different wavelengths will result in photons with different energies. If the bandgap of the PV material is too high, this leads to low-energy photons not contributing anything to electricity generation, but if it is too low, then high-energy photons have their excess energy lost as heat (Friedman, Olson et al. 2011).

To increase electrical conversion efficiency, that is, the amount of sunlight converted in electricity, multiple p-n junctions are stacked on top of each other to harvest more of the solar spectrum. The idea is shown in Figure 3. Sunlight strikes the PV cell, where the higher energy photons are absorbed into the top junction, and the lower energy photons, which cannot be absorbed in the top layer, will pass through, and be absorbed in the bottom junction. This concept can be extended into multiple layers, where each layer has a different bandgap, and will absorb a different part of the solar spectrum. The general classification of such types of cells are called tandem cells or multi-junction (MJ) cells.

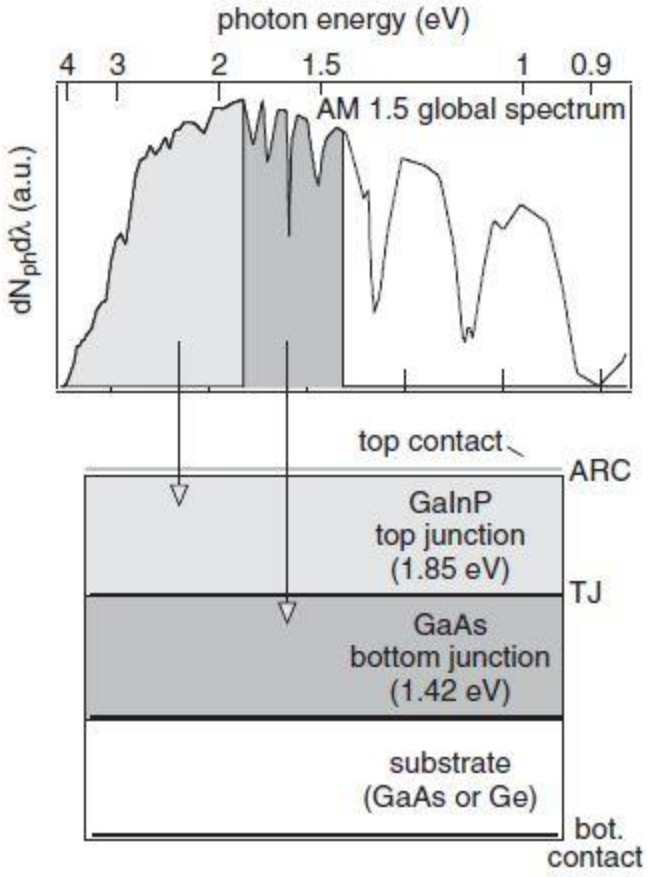

Figure 3: Spectral distribution of sunlight (top), double-junction PV cell (bottom), reprinted from **(**Friedman, Olson et al. 2011)

MJ cells have the highest efficiency amongst solar cells, which is reported at 46% for a CPV system, and 38.8% for a PV system. In comparison, c-Si cells have only reached a maximum of 27.6% for a CPV system, and 25.3% for a PV system (NREL 2017). In terms of cost, MJ solar cells are much more expensive than their c-Si counterparts, due to the more sophisticated and complex setup needed to fabricate them. Therein lies the advantage of the CPV system, which can afford to use the costlier MJ

cells for much high efficiencies while still staying cost effective compared to PV systems.

1.3 Types of concentrators

CPV optics represent a fertile field for innovation, given the young nature of the technology, and the importance of concentrators in the design of a CPV system (Shanks, Senthilarasu et al. 2016). Generally, there are 2 main methods of concentration: reflective and refractive. Reflective systems such as parabolic troughs, are essentially curved concave mirrors that reflect sunlight into a small spot. Refractive systems, such as the Compound Parabolic Concentrator (CPC) bend light inside the structure in a way that focuses it onto a small spot, although in terms of popularity, Fresnel lenses, which use refraction as well as total internal reflection, are a much more popular method of concentration. A representation of these concentrators can be seen in Figure 4.

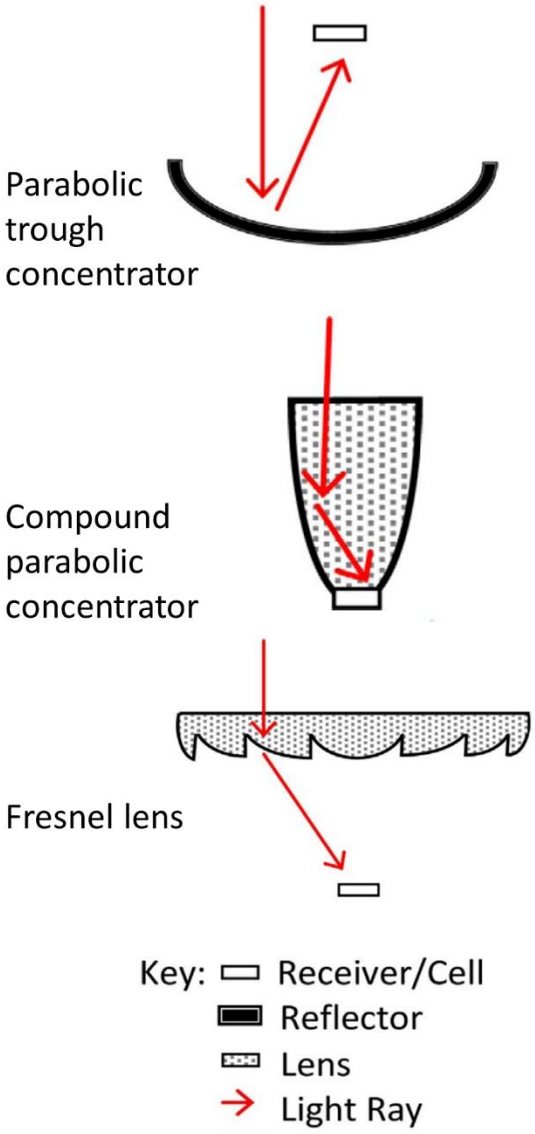

Figure 4: Different concentrator designs, reprinted from (Shanks, Senthilarasu et al. 2016)

The main parameters for characterizing concentrators are optical efficiency, which describes how well a concentrator magnifies sunlight, acceptance angle, which is the maximum angle deviation allowed from the position of the sun in the sky for the concentrator, and finally irradiance uniformity, which describes how even the spread of

sunlight is on the target area. Irradiance uniformity is an important parameter because uneven sunlight spread could result in the formation of hot-spots on the PV cell, and decreased cell efficiency.

Another factor that can affect concentrator design is temperature. In the case of Fresnel lenses, increase in temperature can cause the lens surface to deform, altering its optical efficiency and causing less light to be concentrated (Peharz, Ferrer Rodríguez et al. 2011).

1.4 Cooling of CPV systems

PV cell temperature is an important parameter for power generation. A high cell temperature is undesirable both in terms of power output and structural integrity. As the cell temperature increases, power output is reduced due to increased charge carrier recombination effects in the PV cell (Gray 2011). In the case of PV systems, the effect of temperature is not a big enough concern to require a specific cooling scheme for the system, but this is not the case for CPV systems. Because CPV systems focus energy onto a small area, then there is less space to spread the heat around, and as we can see from Figure 5, cell temperature rises rapidly with concentration ratio, reaching temperatures well beyond normal operating ranges.

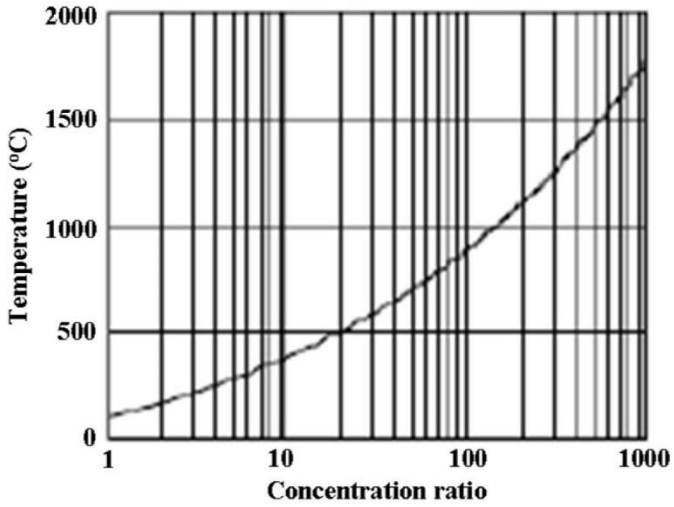

Figure 5: Cell temperature vs. concentration ratio, reprinted from (Zhangbo, Qifen et al. 2009)

Many schemes exist for cooling, ranging from passive cooling, such as using air as a cooling medium, without expending additional energy, or active cooling, for example using a water pump to circulate water for extended contact time. In the case of active cooling, the thermal energy can be partially recovered, for use in other applications, such as domestic hot water in case of a water heating/cooling system.

In the case of high concentrations, active cooling methods are almost always required to keep PV cells within operating temperatures. This complicates CPV setups since they also need sun tracking systems in addition to the active cooling scheme (Jakhar, Soni et al. 2016). For the low concentration CPV systems, passive cooling options are sufficient (Browne, Norton et al. 2015). However, the presence of a concentrator and the degree of this concentration does not necessarily preclude active or passive cooling. The authors of (Micheli, Fernández et al. 2016) model a single triple junction PV cell passively cooled via heat sinks, where concentration levels are between

100-1000 suns. They conclude that a 3×3 mm cell can be cooled to below 80 ˚C using air-cooled aluminum fins.

1.5 Phase Change Materials (PCM)

Phase-change materials (PCM) can be used as a cooling medium in a passive cooling system. PCMs are an alluring cooling option because they can absorb a large amount of heat while maintaining a near constant temperature since this absorption happens via phase change. Popular options include organic (Paraffin/Fatty acids) and inorganic (salt hydrate) PCMs (Sharma, Tahir et al. 2016), which come in a variety of mixes that allow control of their melting points. Melting point is especially a parameter of interest because a CPV-PCM system would most likely be designed to operate in a temperature region close to the melting point.

In CPV systems, the idea behind using PCM is that it absorbs heat during the daytime operation by melting, while in the night, the PCM would release the heat it absorbed back to the environment, solidifying in the process. This would allow for virtually maintenance-free operation.

1.6 CPV market and feasibility

CPV technology is relatively young when compared to tried-and-true flat-plate PV systems, and hence they have not enjoyed the same wide market proliferation. Up to 2016, only 370 MW of CPV power has been installed (Maike Wiesenfarth 2017), and the rate of growth has slowed down due to the falling costs of flat-plate PV systems. HCPV systems, using MJ cells, account for 90% of CPV installations, while LCPV systems, generally using high efficiency c-Si cells, account for the other 10%.

In the Middle East, and specifically the Gulf region, only two (1.1 and 1.0 MW) HCPV systems have been installed, both in Saudi Arabia. In terms of global deployment, CPV systems are of most use in high DNI areas [2000+ kWh/m^2]. As we can see from the solar map of Qatar in Figure 6, the average annual DNI for inland areas is slightly less than the recommended 2000+ kWh/m^2, which in turn causes it to favor LCPV systems rather than HCPV, given that LCPV systems require less tracking, and are able to capture some of the diffuse radiation that the HCPV system cannot.

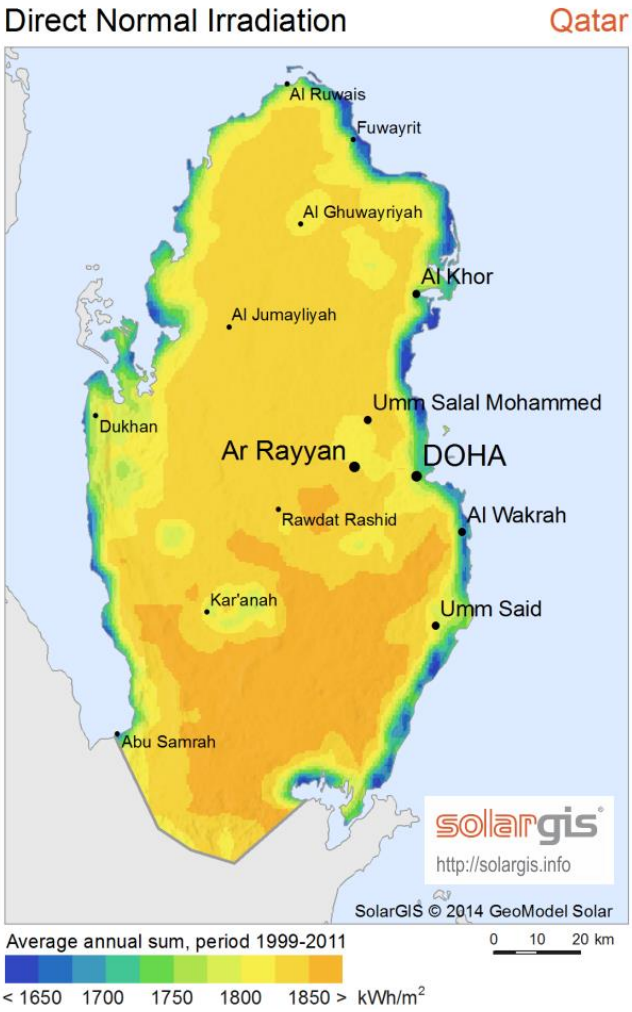

Figure 6: DNI average annual sum for Qatar, reprinted from (Solargis 2017)

1.7 Modeling of PV systems

The modeling of CPV systems is important because it allows the decision maker (e.g. investor) to make an informed call on whether to invest in a certain technology or not. The accuracy of this modeling is vital to make the best decision possible. Since CPV systems, which have a wide range of combinations of technologies (in terms of concentrators, cooling, etc..), are competing against the well-established and mature flat-panel PV technology, accurate and simple modeling is important to give a prediction of power output, temperature profiles and ultimately money per energy unit.

The complete modeling of a CPV-PCM system can usually be split into three parts: optical, thermal, and electrical modeling. The optical modeling deals with determining the amount of incoming sunlight that is absorbed by the PV cell, as the sunlight passes through the transparent cover of the PV cell. Thermal modeling determines the temperature profile of the PV cell and the PCM inside its container. Finally, electrical modeling determines the electrical power generated by the PV cell, which could just be the calculation of the maximum power of the cell, or the calculation of the entire current-voltage (I-V) characteristic curve of the solar cell. Though the calculation of the entire I-V curve is decidedly more involved than the sole calculation of the maximum power, I-V curves are important because in reality, solar cells will not always operate at the maximum power point on the I-V curve, since this depends on the electrical system loads and regulation (Almonacid, Fernández et al. 2015). Therefore, to determine the power output at any point in operation, the full I-V curve is required.

2. OBJECTIVE

The objective of this work is the complete modeling of a CPV-PCM system to predict the most important system outputs, which are the power generation and temperature profile. Naturally, given that a PV system's purpose is to generate electricity, it is vital to know the power output. For the temperature profile, while temperature has a bearing on the power output, it is more important for the evaluation of the PCM, to be able to quantify the effectiveness of the cooling system.

To this goal, we adapt an electrical model, which uses easily obtained information from a PV cell manufacturer's datasheet, and couple it with a previously developed thermal and optical model for a CPV-PCM system (Sarwar, Norton et al. 2016), where the coding for both models is done in MATLAB.

The developed coupled thermal-optical-electrical model is then used for a case study in Qatar, where it is desired to predict the electrical power output and temperature profile of a CPV-PCM system for each month of the year, and as a reference, the CPV-PCM system performance is compared versus a regular, non-concentrated PV system.

3. METHODOLOGY

3.1 Physical model

The CPV-PCM system consists of a non-ideal parabolic trough concentrator, which focuses incoming sunlight onto a c-Si PV cell. The PV cell, which has a Sylgard-182 cover, is attached to an aluminum block that contains a PCM. While the

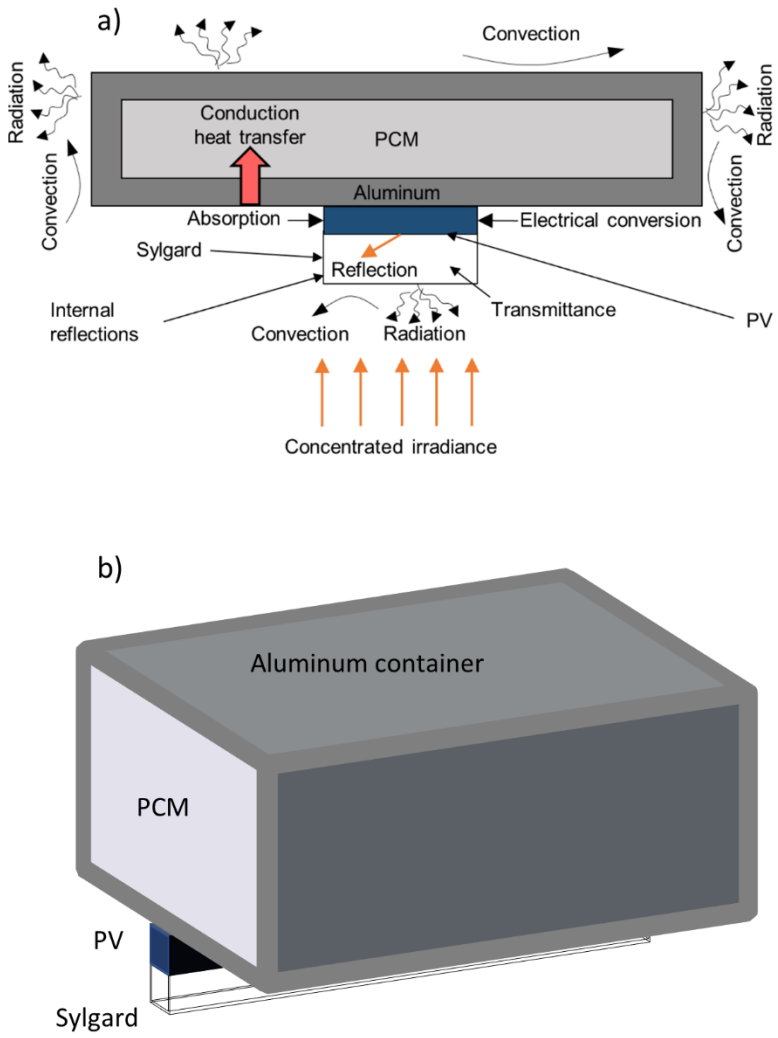

Figure 7: a) 2D overview of CPV-PCM system, **b)** 3D view of CPV-PCM system (both not to scale)

concentrator and its design is not modeled in this work, the choice of a parabolic trough only affects the geometry of the system. The PV cell is placed on the bottom of the PCM container rather than on top, since the parabolic trough would be placed on the underside of the PV cell and PCM container, where it would focus sunlight upwards. A schematic of the system is shown in Figure 7.

As can be seen for Figure 7a, incoming concentrated sunlight (yellow arrow) will either be transmitted through a transparent Sylgard cover, or reflected. Light inside the cover can also undergo internal reflections. Sunlight that is transmitted through the cover will strike the surface of the PV cell, where it absorbed and, according to the cell efficiency, will be converted into DC current. Energy that is not converted into electricity will be lost as heat energy and conducted through the aluminum and into the PCM. In addition, there are also heat losses by convection and radiation from the aluminum container of the PCM.

3.2 Simulation model

3.2.1 Electrical model

3.2.1.1 Introduction

Current-Voltage (I-V) curves provide valuable information to the operation of many electrical components, including solar cells. Given that power is the mathematical multiplication of current and voltage, then I-V curves also give the most important metric for a solar cell, which is the power generation. Hence when we speak of electrical modeling, the result should be the simulation or prediction of the I-V curve for any given solar cell or module at any operating condition.

There are generally two ways to generate I-V curves. One method uses experimentally measured I-V curves for a given solar cell to predict the I-V curve at a condition different from the experimental conditions, through curve fitting, for example using Bilinear interpolation (Almonacid, Rodrigo et al. 2016). The disadvantage of this method is that it requires several experimental results (in the case of Bilinear interpolation, four I-V curves at different operating conditions) which are not always available, and preclude the prediction of I-V curves for other solar cells which do not have I-V curves available for them.

The second method to generate I-V curves uses the concept of the electrically equivalent circuit, which uses traditional electrical circuit components such as current sources, diodes and resistors to approximate the behavior of a real solar cell. One such circuit can be seen in Figure 8, which is popularly called the single diode or five parameter model.

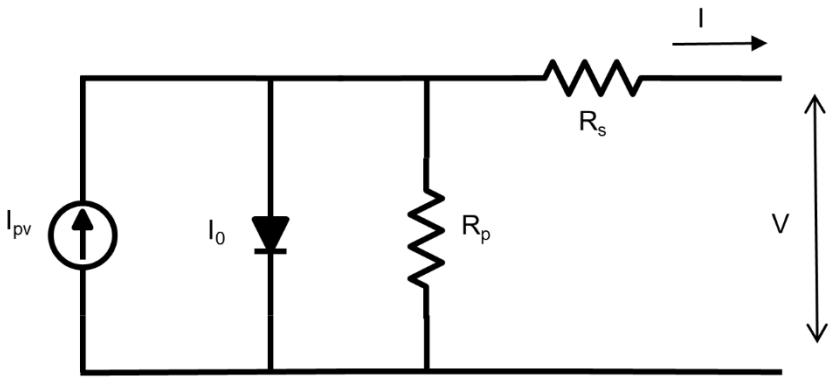

Figure 8: Equivalent circuit for solar cell, reprinted from (Nelson 2003)

The five parameters are the photocurrent I_{pv}, the reverse saturation diode current I_0, the shunt and series resistances R_p and R_s and finally the diode ideality or quality factor a. The equation that describes the relation between current/voltage and the five parameters is:

$$I = I_{pv} - I_0 \left[\exp\left(\frac{V + R_s I}{V_t a}\right)\right] - \frac{V + R_s I}{R_p} \quad (1)$$

where $V_t = N_s k_B T/e$ is the thermal voltage of the array.

If we can find the five parameters, then the solution (i.e. the current and voltage values) becomes a simple matter of numerically solving the transcendental Equation 1 using any root finding method. Here we will use Newton-Raphson method to produce the I-V curve once we solved for the model parameters.

Another equivalent circuit model that is sometimes used is called the double diode or seven parameters model, which uses a similar circuit to the single diode model except for the addition of a second diode in parallel. The extra two parameters are supposed to give a result of greater accuracy, however according to (Humada, Hojabri et al. 2016) and (Ishaque, Salam et al. 2011), the gain in accuracy is mostly seen at the lower irradiance conditions at around 200 W/m^2, which is generally not a concern for CPV systems that operate at high irradiance levels (above 1 sun).

In the end, the increase in complexity for using a double diode model is not worth the gain in accuracy for conditions that are irrelevant for CPV systems, and hence the single diode model is used in this work.

3.2.1.2 Villalva algorithm/Standard test conditions (STC)

The algorithm used is based on the work of (Villalva, Gazoli et al. 2009). This algorithm was chosen since it relies only on data that is provided by PV cell manufacturers, namely the short circuit current I_{sc}, open circuit voltage V_{oc}, current at maximum power I_{mp}, voltage at maximum power V_{mp}, and temperature coefficients of V_{oc} and I_{sc}, which are K_V and K_I respectively.

The importance of the parameters $I_{sc}, V_{oc}, I_{mp}, V_{mp}$ can be seen in Figure 9, as they represent significant points on the I-V curve. I_{sc} represents the maximum current, when the electrical circuit is shorted (i.e. a very low resistance load is added). At this point no power can be extracted because there is zero voltage. V_{oc} represents the maximum voltage, where the electrical circuit is left open (i.e. a very high resistance load is added), and similarly to I_{sc}, no power can be extracted at the V_{oc} point because there is zero current. I_{mp} and V_{mp} represents the current and voltage where maximum power is extracted.

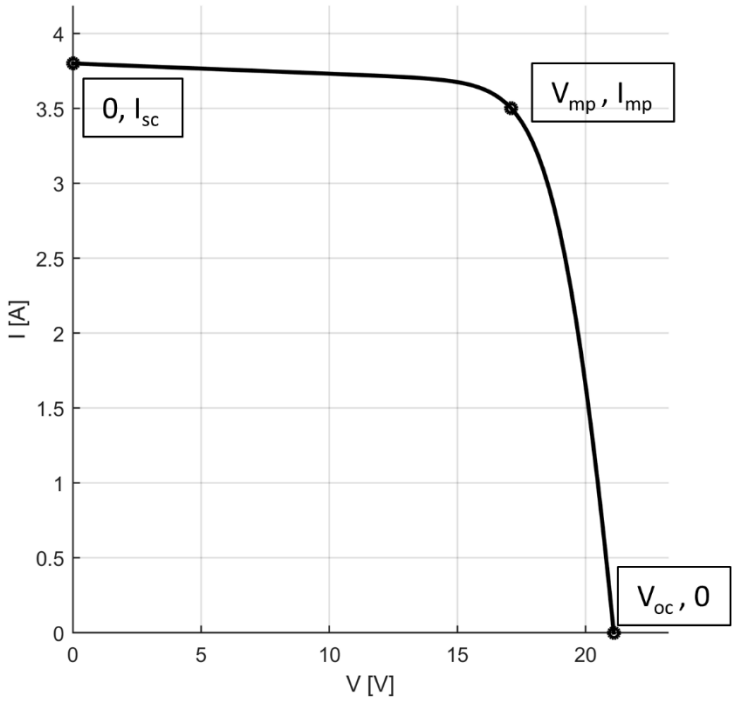

Figure 9: Typical I-V curve

The Villalva algorithm is also simple to implement and accurate compared to other five-parameter model algorithms. (Ciulla, Lo Brano et al. 2014). Additionally, the model output can be computed very rapidly, since the algorithm is split into two parts, the first and slow part is the iterative procedure that is essentially done only once per PV cell, and the second and fast part which uses simple algebraic equations to predict I-V curves at any other operating condition for that same PV cell.

The algorithm starts off by calculating the five parameters at standard test conditions (STC), which are a cell temperature of 25 ℃ and incident irradiance of 1000 W/m^2, then it applies modifications or corrections to certain parameters so that they predict the I-V curve at any condition other than STC.

The algorithm iterative logic can be seen in Figure 10. The algorithm relies on the fact that there is only one pair of values of R_s and R_p for which the maximum

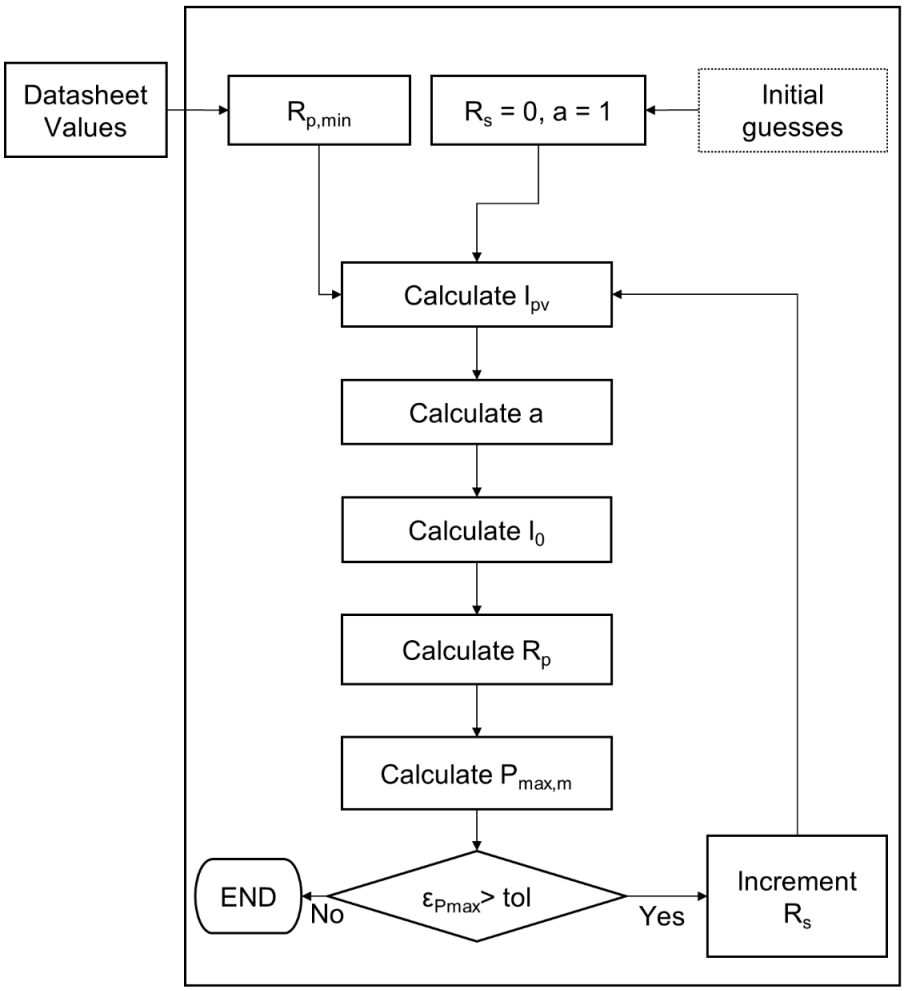

Figure 10: Flowchart for Villalva algorithm for standard conditions only

experimental power $P_{max,e}$ is equal to the maximum power calculated by the model $P_{max,m}$. To find the value of this pair R_p, R_s, we use an iterative method with the condition that $P_{max,m} - P_{max,e} < \varepsilon_{tol}$, where ε_{tol} is the defined tolerance (arbitrarily set at 0.0001).

Initially, R_s is set to 0, and the minimum value of R_p, $R_{p,min}$ is calculated by the following equation:

$$R_{p,min} = \frac{V_{mp}}{I_{sc,n} - I_{mp}} - \frac{V_{oc,n} - V_{mp}}{I_{mp}} \quad (2)$$

This equation is derived from the slope of the line segment between the short-circuit and maximum power points on the I-V curve, which makes it a good initial guess for the value of R_p.

With these initial values set, the algorithm loop starts, where in each iteration, the value of R_s is incremented by a value (set at 0.001).

For the ideality factor a, it is assumed to be between 1 and 1.5 (Villalva, Gazoli et al. 2009). Because this value is empirical, we initially set it to equal 1, however the ideality factor can be calculated using the following equation, as suggested by (Femia 2013)

$$a = \frac{K_V - \frac{V_{oc}}{T_{STC}}}{N_s * V_t * (\frac{K_I}{I_{pv}} - \frac{3}{T_{STC}} - \frac{E_{gap}}{k_B * T_{STC}^2})} \quad (3)$$

where N_s is the number of cells in series for the module, T_{STC} is the temperature at standard conditions (298 K), k_B is the Boltzmann constant ($1.3806503*10^{-23}$ J/K), and E_{gap} is the bandgap energy for crystalline silicon ($1.8*10^{-19}$ J). This only leaves I_{pv} and I_0 as unknowns.

A common assumption is to have the photocurrent $I_{pv} \approx I_{sc}$ because in reality, the series resistance R_s is low and the parallel resistance R_p is high (Villalva, Gazoli et

al. 2009), but in this algorithm, we can take advantage of the values found for R_s and R_p to calculate I_{pv}:

$$I_{pv} = \frac{R_p + R_s}{R_p} I_{sc,n} \tag{4}$$

As the solution of the algorithm converges to the correct R_p, and R_s values, so too will the value of I_{pv} improve in accuracy.

From Equation 1, we can derive the value of diode current I_0, by setting $I = 0$ and $V = V_{oc}$. This aims to match the experimental open circuit voltage V_{oc} with the model calculated V_{oc}. Hence I_0 is calculated by the following equation:

$$I_0 = \frac{I_{pv} - \frac{V_{oc}}{R_p}}{\exp\left(\frac{V_{oc}}{V_t a}\right) - 1} \tag{5}$$

Finally, we calculate R_p based on the algorithm objective which is $P_{max,m} = P_{max,e}$, through the following equation:

$$R_p = \frac{V_{mp}(V_{mp} + I_{mp}R_s)}{V_{mp}I_{pv} - V_{mp}I_0 \exp\left[\frac{\left(V_{mp} + I_{mp}R_s\right)}{N_s a}\frac{e}{k_B T}\right] + V_{mp}I_0 - P_{max,e}} \tag{6}$$

The algorithm will then loop until the condition $P_{max,m} - P_{max,e} < \varepsilon_{tol}$ is met.

Now that all five parameters are found, we can simply construct an I-V curve by solving Equation 1 numerically, using Newton-Raphson method to find the values of current I for a set of voltage values V.

3.2.1.3 Villalva algorithm/non-STC

The model so far can successfully provide I-V curves, but only at the standard test conditions (25 ℃ and 1000 W/m^2). For use at other temperatures and irradiances, we calculate corrections to I_{pv} and I_0, on the assumption that I_{pv} is a linear function of irradiance, and I_0 is a function of temperature, while R_p, R_s and a are constants.

First, we correct the short circuit current as a function of temperature and irradiance, and we correct open circuit voltage as a function of temperature, using the datasheet temperature coefficients:

$$I_{sc} = (I_{sc,n} + K_I \Delta T)\frac{G}{G_n} \tag{7}$$

where ΔT is the temperature difference (from nominal temperature), G, G_n are the actual irradiance and nominal irradiance respectively.

$$V_{oc} = (V_{oc,n} + K_V \Delta T) \tag{8}$$

The photocurrent I_{pv} is corrected using Equation 4, except that instead of $I_{sc,n}$ we use the new value for I_{sc}

The diode current I_0 is corrected using Equation 5, except we use the new V_{oc} and I_{pv} values.

To obtain the new, temperature and irradiance corrected, I-V curves, we use the same numerical (Newton-Raphson) method to construct the I-V curve.

From the I-V curves, it is straightforward to obtain P-V curves and ultimately derive the maximum power for the given setup.

3.2.1.4 Improvement to Villalva algorithm/non-STC

The original algorithm by Villalva was only verified for data for flat-plate PV modules, which is not a surprise as its original purpose was the modeling of non-concentrator PV systems. However, we see that if the algorithm is used as it is for concentrated irradiance conditions, the model does not do a good job of predicting the power output. This can be seen from Figure 11, where the original algorithm fails to produce the correct I-V curve because the series resistance R_s is kept constant.

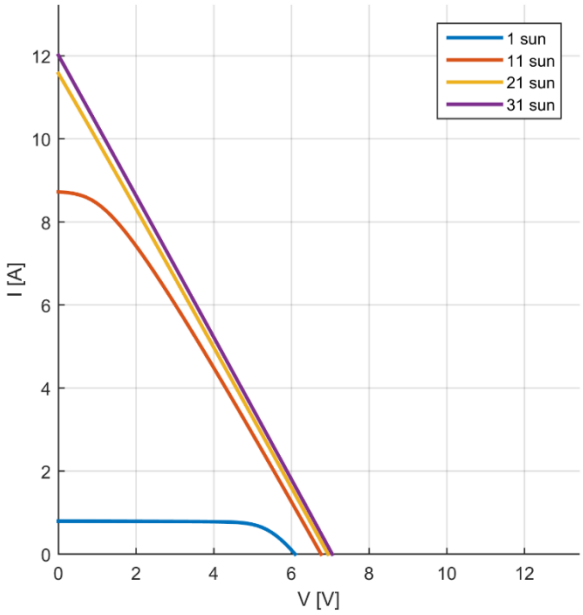

Figure 11: I-V curve for 1 to 31 suns, original Villalva algorithm

The series resistance R_s should also be corrected, as observed from experimental data for irradiances below 1000 W/m^2 in (Priyanka, Lal et al. 2007), and for irradiances from two to 10 suns in (Khan, Baek et al. 2014), where it is shown experimentally that the series resistance decreases as irradiance increases. To account for the series

resistance change, we use a suggestion in another five parameter model by (Lo Brano, Orioli et al. 2010), where it is proposed that the series resistance changes as follows

$$R_s = \frac{R_{s,n}}{G/G_n} \tag{9}$$

Running the same algorithm with R_s modified to change with irradiance, we can see that the same module simulated to give I-V curves in Figure 11 is now being properly represented as seen in Figure 12.

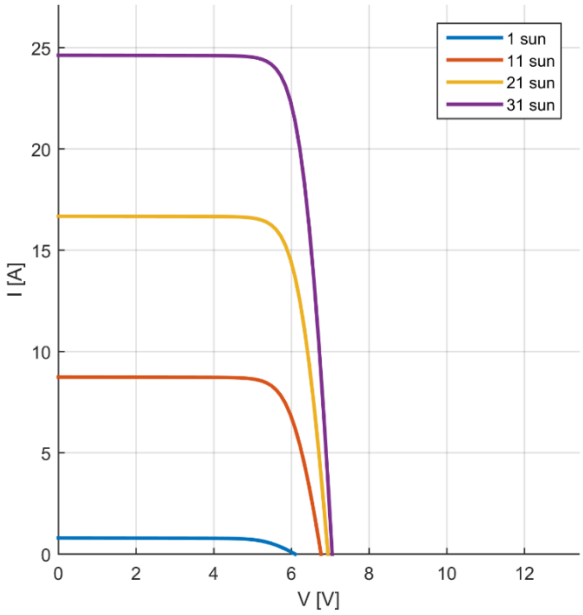

Figure 12: I-V curve for 1 to 31 suns, modified Villalva algorithm

3.2.2 Thermal-Optical model

For the thermal-optical model, we use a finite element based heat transfer model, developed via a two-dimensional (2-D) differential heat diffusion equation considering heat losses via convection and radiation. The optical behavior is simulated using a Fresnel equations method (Sarwar, Norton et al. 2016). As mentioned in the objective, this model has been developed in-house by the authors of the paper referenced in the previous paragraph, and thus there will be no detailed discussion of it in this work. However, for the sake of completeness, a general overview and description of the thermal-optical model is offered below.

The fundamental (2-D) equation that describes the conduction of heat across the PCM (and PCM container boundaries) is:

$$\rho c \frac{\partial T}{\partial t} - \left[\frac{\partial}{\partial x_i}\left(k_{ij}\frac{\partial T}{\partial x_j}\right)\right] = 0 \tag{10}$$

The next two equations describe the convection and radiation heat losses respectively at the system boundaries:

$$H = h_c A \Delta T \tag{11}$$

$$R = h_r A \Delta T \tag{12}$$

Now we can construct the energy balance for the system using Equations (10-12). Given that Equation 10 is a partial differential equation (PDE), we will use the finite element method (FEM) to solve the energy balance. As part of this method, we first need to obtain the weak formulation for the energy balance, where we multiply the energy balance by a test function T , integrated over the domain, then apply the Green-

Gauss and divergence theorems to obtain the simplified, weak formulation. Equation 13 shows the result of this process:

$$\int_{\Omega} \delta T \rho c \frac{\partial T}{\partial t} \partial\Omega + \int_{\Omega} \left[k_{11} \frac{\partial \delta T}{\partial x_1} \left(\frac{\partial T}{\partial x_1} \right) \right] + \left[k_{22} \frac{\partial \delta T}{\partial x_2} \left(\frac{\partial T}{\partial x_2} \right) \right] \partial\Omega - \int_{\Gamma} \delta T q \partial A + \int_{\Gamma} \delta T (H + R) \partial A = 0 \quad (13)$$

Next, we discretize our system, which will be done using an 8-node Serendipity element. We use the chain rule to transform Equation 13 from physical coordinates to natural coordinates. This results in Equation 14:

$$\mathbf{M}\dot{T} + \mathbf{K}T - \boldsymbol{q} + (\mathbf{H} + \mathbf{R})T = 0 \quad (14)$$

where $\mathbf{M}, \mathbf{K}, \mathbf{H}, \mathbf{R}$ and $\boldsymbol{q}$ are the mass, conductivity, convection, radiation, and irradiance matrices, and $\dot{T}$ is the time-derivative of temperature. The matrices are calculated as such:

$$\mathbf{M} = \int_{-1}^{1} \int_{-1}^{1} \rho c N^T N |J| h \partial\xi_1 \partial\xi_2 \quad (15)$$

$$\mathbf{K} = \int_{-1}^{1} \int_{-1}^{1} B^T k B |J| h \partial\xi_1 \partial\xi_2 \quad (16)$$

$$\mathbf{H} = \int_{-1}^{1} h_c N^T N |J_i| h \partial\xi_{1\ or\ 2} \quad (17)$$

$$\mathbf{R} = \int_{-1}^{1} h_r N^T N |J_i| h \partial\xi_{1\ or\ 2} \quad (18)$$

$$\boldsymbol{q} = \int_{-1}^{1} q N^T N |J_i| h \partial\xi_{1\ or\ 2} \quad (19)$$

where N is the 8-node Serendipity element, B is the B-operator, ξ is the natural coordinate, J is the Jacobian matrix and h is the system width. For the physical

discretization, we use the direct addition of components method to assemble all elements. For the temporal discretization, we use a Crank-Nicholson scheme.

Equations 17 and 18 also use h_c and h_r, which are the convection and radiation heat transfer coefficients respectively. These are calculated at each time step using the following equations:

$$h_c = 2.9v + 4.5 \tag{20}$$

$$h_r = \sigma \varepsilon F \left(\frac{T^4 - T_{sky}^4}{T - T_{sky}} \right) \tag{21}$$

where v is the air velocity, σ is the Stefan-Boltzmann constant, ε is the emissivity, T_{sky} is the sky temperature and F is the view factor. According to (Hoang, Bourdin et al. 2014), T_{sky} is to be calculated as follow:

$$T_{sky} = T_{amb} - 20 \text{ K} \tag{22}$$

where T_{amb} is the ambient temperature. For the view factor, the following equation calculates it:

$$F = (1 + \cos(s)) \tag{23}$$

where s is the panel inclination. In the case of indoor calculations, natural convection is considered while room temperature is taken as the ambient temperature.

To account for the latent heat effect of the PCM (used in Equation 15), we use an effective heat capacity method (Lamberg, Lehtiniemi et al. 2004), which uses the following equations:

$$\begin{aligned} c_e &= c_s && T < T_1 \\ c_e &= c_s + \frac{L}{T_2 - T_1} && T_1 \le T \le T_2 \\ c_e &= c_l && T > T_2 \end{aligned} \tag{24}$$

where c_e is the PCM effective heat capacity, c_s and c_l are the solid and liquid PCM heat capacities, L is the latent heat of fusion for the PCM, and T_1 and T_2 are melting onset and solidification temperatures of the PCM.

As shown in Figure 7, irradiance that is incident on the PV glass cover undergoes several reflections and absorptions in the cover until it is absorbed into the PV cell itself. Reflectance, transmittance and absorptance of this system is modeled using Fresnel equations (Hecht 2002):

$$rf = \frac{1}{2}\left(rf_{\parallel} + rf_{\perp}\right) \qquad rf_{\perp} = -\frac{\sin(\theta_i - \theta_t)}{\sin(\theta_i + \theta_t)} \qquad rf_{\parallel} = \frac{\tan(\theta_i - \theta_t)}{\tan(\theta_i + \theta_t)}$$

$$\tau = \frac{1}{2}(\tau_{\parallel} + \tau_{\perp}) \qquad \tau_{\perp} = \tau_a\left(\frac{1 - rf_{\perp}}{1 + rf_{\perp}}\right)\left(\frac{1 - rf_{\perp}^2}{1 + rf_{\perp}^2\tau_a^2}\right) \qquad \tau_{\parallel} = \tau_a\left(\frac{1 - rf_{\parallel}}{1 + rf_{\parallel}}\right)\left(\frac{1 - rf_{\parallel}^2}{1 + rf_{\parallel}^2\tau_a^2}\right)$$

$$\alpha = \frac{1}{2}(\alpha_{\parallel} + \alpha_{\perp}) \qquad \alpha_{\perp} = (1 - \tau_a)\left(\frac{1 - rf_{\perp}}{1 + rf_{\perp}\tau_a}\right) \qquad \alpha_{\parallel} = (1 - \tau_a)\left(\frac{1 - rf_{\parallel}}{1 + rf_{\parallel}\tau_a}\right)$$

$$\tau_a = e^{-\frac{Kx}{\cos\theta_t}} \tag{25}$$

Using Snell's refractive law, we calculate the transmittance angle θ_t from an incidence angle θ_i. In the case of indoor calculations, the incident irradiance can be assumed to be normal to the cover. For outdoor calculations, we use a formulation by (Hoang, Bourdin et al. 2014) to calculate the incident angle, as well as the sun declination angle δ and hour angle ω. Equation 26 summarizes this below:

$$\cos\theta_i = \sin\delta \times \sin l \times \cos s - \sin\delta \times \cos l \times \sin s \times \cos\varphi + \cos\delta \times \cos l \times \cos s \times \cos\omega + \cos\delta \times \sin l \times \sin s \times \cos\varphi \times \cos\omega + \cos\delta \times \sin s \times \sin\varphi \times \sin\omega$$

$$\delta = 0.38 + 23.26\sin\left(\frac{2\pi J'}{365.24 - 1.395}\right) + 0.37\sin\left(\frac{4\pi J'}{365.24 - 1.457}\right)$$

$$\omega = 15 \times \left(H_l - \Delta H_l + \Delta H_g - E - 12\right)$$

$$E = 7.5 \times \sin\left(\frac{2\pi J'}{365.24} - 0.03\right) + 0.99 \times \sin\left(\frac{4\pi J_u}{365.24} + 0.35\right) \quad (26)$$

where J' is the rank of day after the first of January 2013, J_u is the Julian day of the year, H_l is the local time, ΔH_l is the time lag between a given time zone and UTC, and ΔH_g is the time lag due to longitude variation.

3.2.3 Coupling of models

Coupling of the three models is required because the thermal and electrical models depend on the optical model, and the electrical model depends on both the thermal and optical model. Figure 13 shows an overview of the inputs and outputs for the different models.

First, we start with the optical model, which, after calculating the reflectance, transmittance and absorptance, will output the incident irradiance upon the PV cell after optical losses:

$$q_{aol} = (1 - rf - \alpha)G \quad (27)$$

Next, part of the irradiance incident on the PV cell will be converted into electricity, depending on the PV cell conversion efficiency, therefore we wish to

calculate the fraction of irradiance that is used for electrical conversion, or q_e, as shown in Equation 28.

$$q_e = [\eta + \mu(T - T_{amb})]q_{aol} \tag{28}$$

where η is the PV cell efficiency and μ is the maximum power temperature coefficient. Finally, this leaves the part of the irradiance that is conducted into the PCM, which is calculated by Equation 29.

$$q = q_{aol} - q_e \tag{29}$$

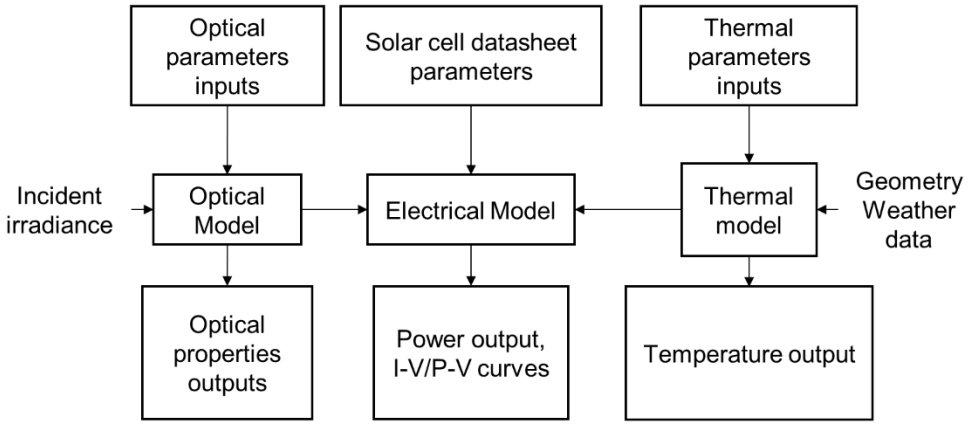

Figure 13: Coupled Electrical-Thermal-Optical model overview

4. MODEL VALIDATION

4.1 Electrical model validation and limitations

4.1.1 Electrical model validation

The electrical model was validated by comparing the I-V curves generated by the model, with those provided by four different modules, two from Kyocera (Kyocera) (Kyocera), one from Hyundai (Hyundai 2014) and one from Suntech Power (Suntech 2016).

As can be seen from Figure 14 to Figure 20, the result shows that the I-V curves (and one P-V curve) generated from the model are consistent with manufacturer's data, where the error was less than 6.5% in all cases.

Because manufacturers seldom provide the numerical data that produced the I-V curve, the software Graph Grabber (Quintessa 2017) is used to extract numerical info from the image file of the published I-V curve. This method does require manual tracing of the lines that constitute the I-V curve, and hence some errors, although minimal, can be expected.

For CPV systems, there was not much experimental data available in the literature for CPV systems with concentration ratios in the range of 5-30 suns, the data needed for the complete verification being the I-V curve for STC (1 sun) and at a concentrated level. The only complete piece of information that was found and is used for verification in this work is for a CPV cell operating at approximately 3 suns (Sweet, Rolley et al. 2016).

To quantify the degree of agreement between the simulated and experimental results, we calculate the mean absolute error (MAE) as follows:

$$MAE = \frac{1}{N_{sam}} \sum_{i=1}^{N_{sam}} \left| \frac{I_{sim} - I_{exp}}{I_{exp}} \right| \tag{30}$$

where N_{sam} is the number of samples, I_{sim} is the simulated current value, and I_{exp} is the experimental current value. A summary of the validation results can be seen in Table 1.

Table 1: Summary of electrical model validation results

Module/cell	Irradiance MAE	Temperature MAE
Hyundai HiS-S275RG	--	3.12%
Kyocera KC175GHT-2	5.47%	4.92%
Kyocera KC200GT	6.40%	3.02%
Suntech STP275S	4.24%	--
CPV cell	6.42%	--

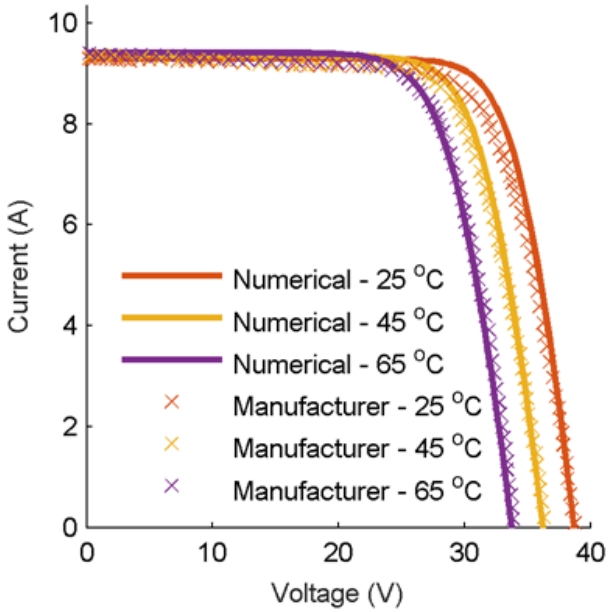

Figure 14: Comparison of modeled and manufacturer's I-V curves for Hyundai HiS-S275RG at 1000 W/m^2, solid line represents simulated data, and crossed line represents manufacturer data

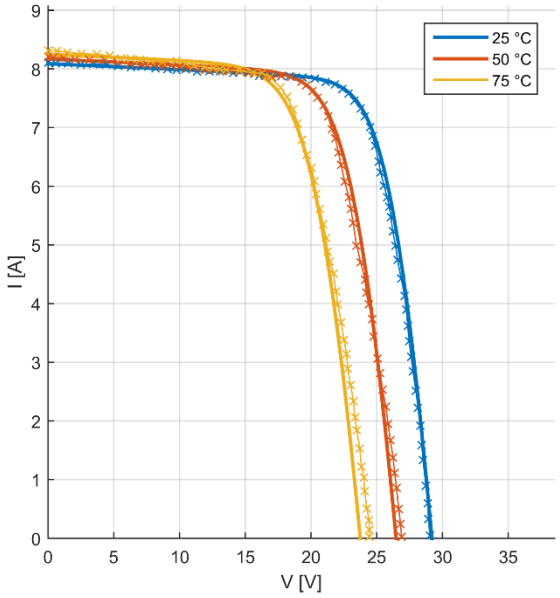

Figure 15: Comparison of modeled and manufacturer's I-V curves for Kyocera KC175GHT-2 at 1000 W/m^2, solid line represents simulated data, and crossed line represents manufacturer data

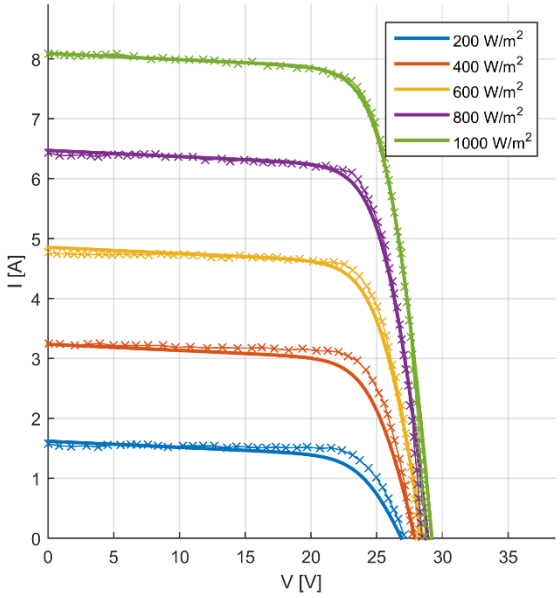

Figure 16: Comparison of modeled and manufacturer's I-V curves for Kyocera KC175GHT-2 at 25 °C, solid line represents simulated data, and crossed line represents manufacturer data

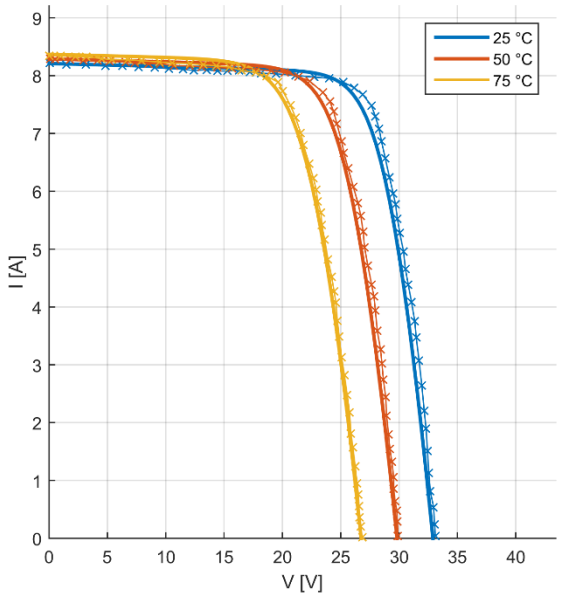

Figure 17: Comparison of modeled and manufacturer's I-V curves for Kyocera KC200GT at 1000 W/m^2, solid line represents simulated data, and crossed line represents manufacturer data

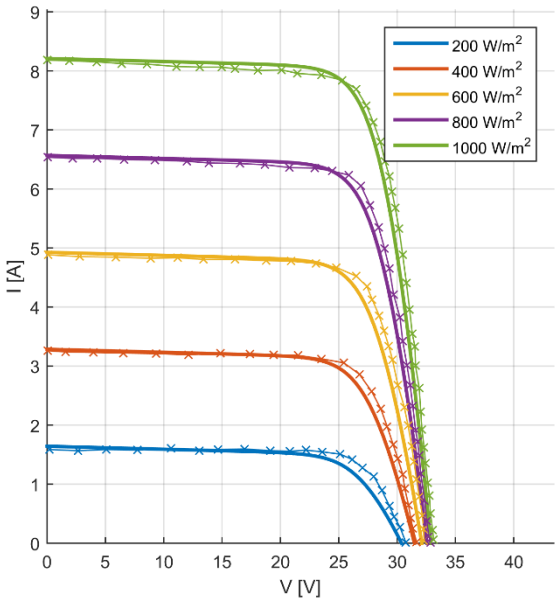

Figure 18: Comparison of modeled and manufacturer's I-V curves for Kyocera KC200GT at 25 °C, solid line represents simulated data, and crossed line represents manufacturer data

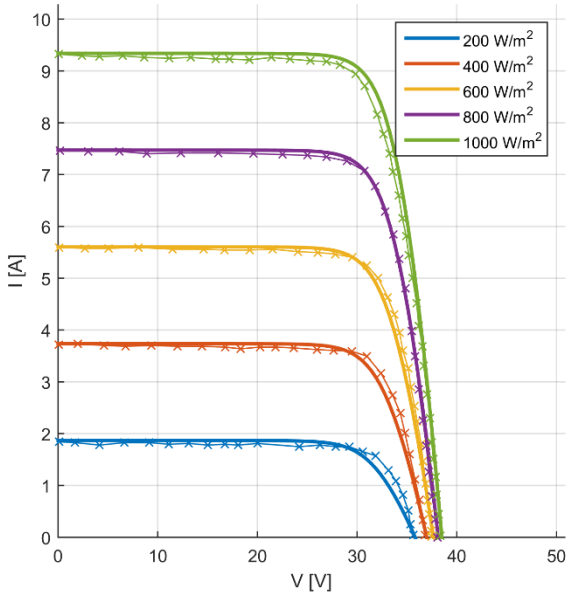

Figure 19: Comparison of modeled and manufacturer's I-V curves for Suntech STP275S at 25 °C, solid line represents simulated data, and crossed line represents manufacturer data

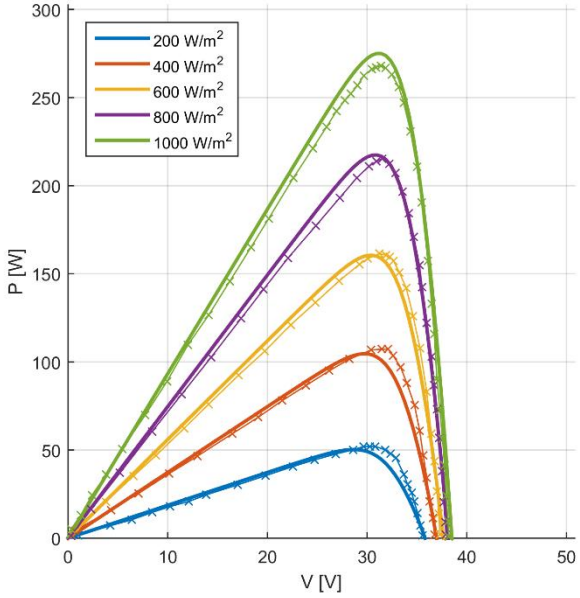

Figure 20: Comparison of modeled and manufacturer's P-V curves for Suntech STP275S at 25 °C, solid line represents simulated data, and crossed line represents manufacturer data

The electrical model was also used to predict the output of CPV cell which uses a Crossed Compound Parabolic Concentrator (CCPC) to focus sunlight at an optical concentration level of 3.15, as described in (Sweet, Rolley et al. 2016). The concentration level was calculated from the short-circuit current for PV and CPV cell, on the assumption that the short circuit current scales linearly with irradiance, which is the same assumption made in the algorithm used for the electrical model. The I-V and P-V

curves can be seen in Figure 21 and Figure 22. The model generally shows good agreement with the experimental result.

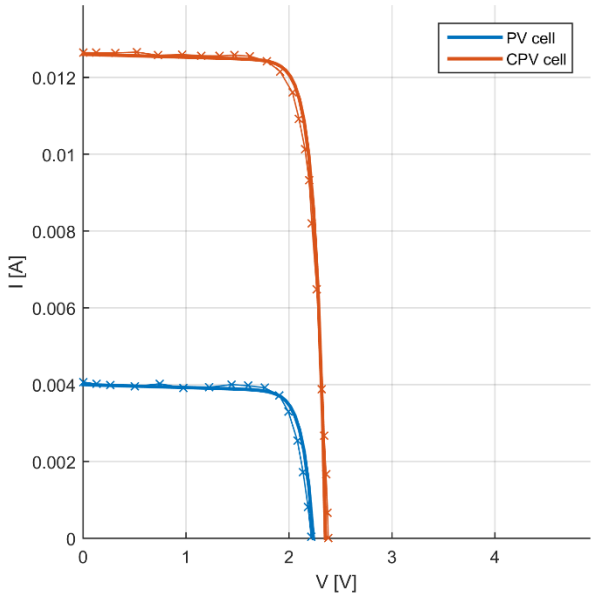

Figure 21: Comparison of modeled and experimental I-V curves for CPV cell at 25 °C, solid line represents simulated data, and crossed line represents experimental data

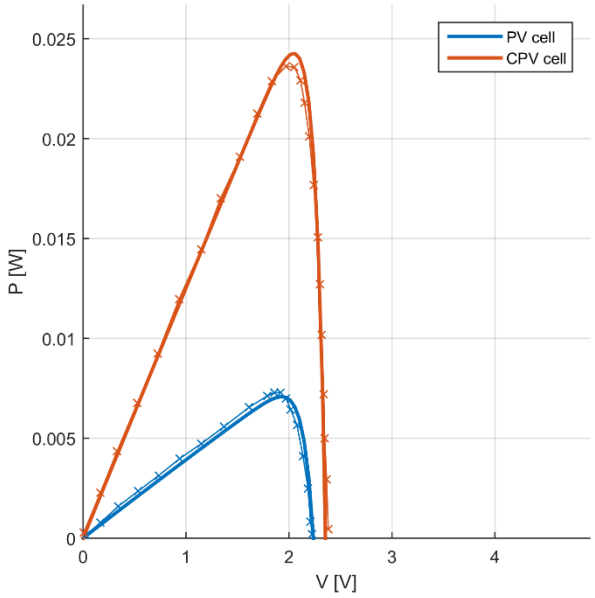

Figure 22: Comparison of modeled and experimental P-V curves for CPV cell at 25 °C, solid line represents simulated data, and crossed line represents experimental data

4.1.2 Electrical model limitations

Theoretically, the electrical model can predict the correct I-V curve at any condition (i.e. temperature and irradiance), but practically, it is the amount of available and comparable experimental data that limits the support for this model. In this case, the model was sufficiently validated against temperatures from 25 °C to 75 °C and irradiances from 200-3150 W/m^2 (0.2 to 3.15 suns).

It is not only the lack of data which limits the model, but also the operating conditions at which PV or CPV systems are realistically supposed to operate at. We can see from solar module datasheets like (Suntech 2016), the operating temperature range is between -40 °C and 85 °C, hence it is not realistic to account for an operating temperature of 150 °C, as that would exceed safety limits. For higher irradiances (e.g.

10-50 suns), it is the lack of experimental data which limits a better validation for the model.

4.2 Thermal-Optical model validation

The thermal-optical model has been previously verified with indoor experiments in (Sarwar, Norton et al. 2016) and outdoor experiments in (Hasan, Sarwar et al. 2017). Figure 23 and Figure 24 show that results from both experiments agree with simulation results. The details of the validations can be found in their respective papers.

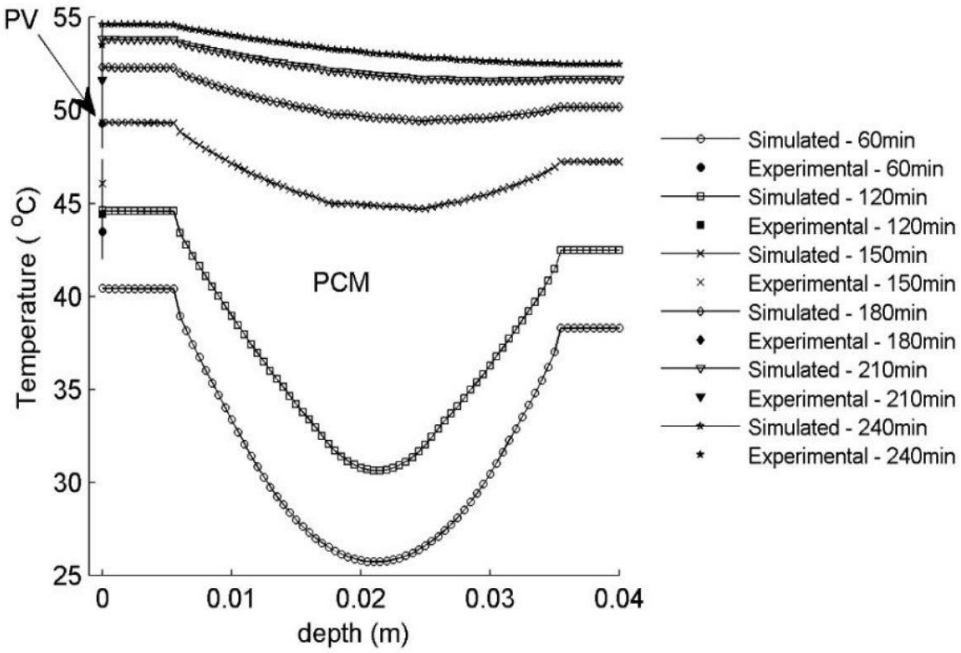

Figure 23: Comparison between indoor experimental results with simulation for thermal-optical model

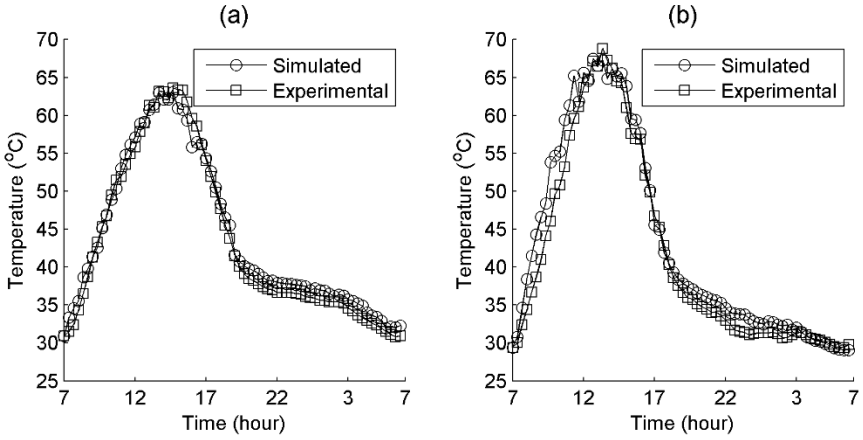

Figure 24: Comparison between outdoor (UAE) experimental results with simulation for thermal-optical model, **a)** PV-PCM system in August, **b)** PV only system in September

5. RESULTS AND DISCUSSION

5.1 Case study – Effect of PCM properties (2-4 suns)*

We examined the effect of the thermal conductivity, latent heat of fusion, melting point for the PCM, and the ambient temperature on power generation and its temporal variation (Jawad Sarwar 2017). The set of parameters used for analysis is specific to this section only, and is shown in Table 2. The system consists of 15 PV cells in series, each has an aluminum PCM container attached with the dimensions 156.4 × 156.4 × 38 mm^3. A glass cover of thickness 5 mm covers the PV cell, and the thickness of the PCM container is 3 mm. The concentration ratios considered are from two to four suns.

It should be noted that for the modules examined, we sometimes want to change the configuration of the model to include fewer solar cells, or to have solar cells of different sizes being simulated. This requires a change in the model input to accommodate for this fact, specifically $V_{oc}, V_{mp}, I_{sc}, I_{mp}$ would all have to be modified. To simulate solar cells that have a smaller surface area, the currents I_{mp}, I_{sc} are assumed to scale linearly with cell surface area, for example if the current for a cell with surface area of 10 cm^2 is 2 amperes, then the current for a cell with surface area of 5 cm^2 with the same properties would be 1 ampere, with every other property (voltages namely) staying the same (Wenham, Green et al. 2012). To simulate a solar module with fewer

* © 2017 IEEE. Reprinted, with permission, from Jawad Sarwar, Ahmed E. Abbas, Konstantinos E. Kakosimos, "Effect of the thermophysical properties of a phase change material on the electrical output of a concentrated photovoltaic system", 44th IEEE Photovoltaic Specialist Conference, Washington DC, USA, June 2017

cells than listed in the datasheet, we assume the voltages V_{mp}, V_{oc} scale linearly with the number of cells connected in series, which is a fair assumption if the individual solar cells in the module are matched (i.e. identical) (Femia 2013).

The temporal variation result for three suns is shown in Figure 25, which considers 4 hours of system operation. It is found that an increase in thermal conductivity of the PCM helps the CPV system in achieving the steady state more quickly as compared to a PCM having a low thermal conductivity. The increase in ambient temperature and melting temperature when other parameters are kept constant results in a decrease in electrical output. The change in the heat of fusion of the PCM produces a negligible effect on the electrical output of the CPV system.

Table 2: Parameters used for system analysis in Section 5.1 only

Electrical Parameters – Hyundai S275RG Solar Module										
Datasheet Values				**Single Diode Model Values**						
P_{max}	275 W			I_{pv}	9.301709 A					
I_{mp}	8.8 A			I_0	$4.013 * 10^{-10}$ A					
V_{mp}	31.3 V			R_s	0.075 Ω					
I_{sc}	9.3 A			R_P	955.373 Ω					
V_{oc}	38.7 V			a	1.05					
I_{sc} temperature coefficient	0.032 %/K			No. of series cells	15					
V_{oc} temperature coefficient	-0.32 %/K									
Input thermal parameters for the model										
Property	**Steps**									
	1	**2**	**3**	**4**	**5**	**6**	**7**	**8**	**9**	**10**
Thermal conductivity ($Wm^{-1}K^{-1}$)	2	4	6	8	10	12	14	16	18	20
Melting temperature (^oC)	45	47.5	50	52.5	55	57.5	60	62.5	65	67.5
Heat of fusion ($kJkg^{-1}$)	150	160	170	180	190	200	210	220	230	240
Ambient temperature (^oC)	25	30	32.5	35	37.5	40	42.5	45	47.5	50

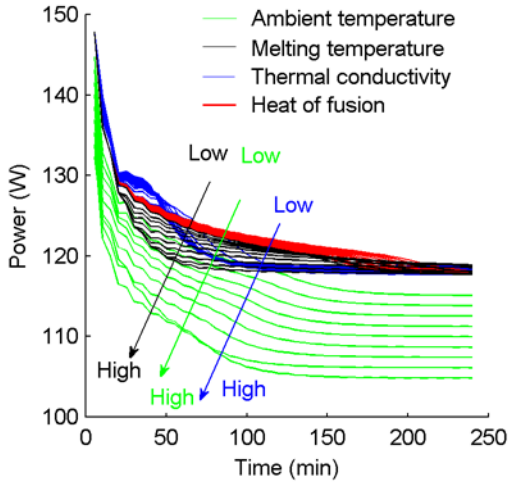

Figure 25: Power of photovoltaic at different ambient temperature, thermal conductivity, heat of fusion and melting point at concentration ratio of 3x

The energy produced for one hour (kWh) was calculated and normalized for each set of simulations to compare their output (Figure 26). We can see that the ambient temperature has the biggest effect on power generation; the power loss is almost 10% with an increase from 25 °C to 50 °C at all flux levels. The change in the heat of fusion, melting temperature, and ambient temperature affects the energy production linearly, but there is a non-linear change in case of thermal conductivity. There is a negligible increase in the energy output of the CPV system, which is found with an increase in thermal conductivity of the PCM beyond 12 $Wm^{-1}K^{-1}$. An overall 3.5% increase in energy output is found for thermal conductivity while the corresponding increase is found as 2% for change in melting temperature and the latent heat of fusion.

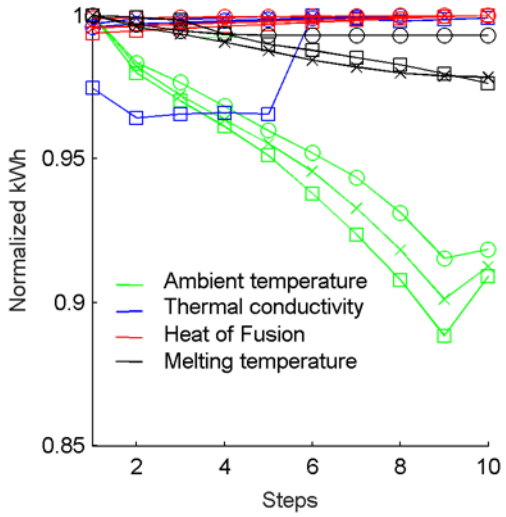

Figure 26: Normalized energy (kWh) against selected parameters after 1 hour of operation. ○, ×, □ points denote 2x, 3x and 4x solar concentration respectively

In addition, we also wanted to investigate the effect of varying the thermo-physical properties of the PCM (i.e. thermal conductivity, heat of fusion, melting point) on the maximum power generation at certain ambient temperatures, with the aim of finding out generally what the appropriate PCM would be for different climates. This study was performed for a system with 4x concentration ratio. As we can see from Figure 27, the optimal PCM (marked with a circle) is different for varying ambient temperatures. At an ambient temperature of 25 °C, there are two configurations for the optimal PCM: high heat of fusion (210-240 $kJkg^{-1}$) and a low thermal conductivity (2-5 $Wm^{-1}K^{-1}$), or a low heat of fusion (150-170 $kJkg^{-1}$) and high thermal conductivity (15-20 $Wm^{-1}K^{-1}$). In both optimal PCM cases for 25 °C ambient temperature, a low melting point (45-50 °C) is desirable.

The optimal PCM has similar properties when looking at ambient temperatures of 30 °C, 35 °C and 40 °C, which are high heats of fusion, low thermal conductivities, and low melting temperatures. When the ambient temperature increases to the 45 °C and 50 °C range, high heats of fusion, high thermal conductivities and high melting temperatures are favored. The difference between an unoptimized PCM and the optimal PCM was found to be 13%, hence the increase in electrical yield of a CPV cell at 4x can be up to 13% after the selection of an optimal PCM.

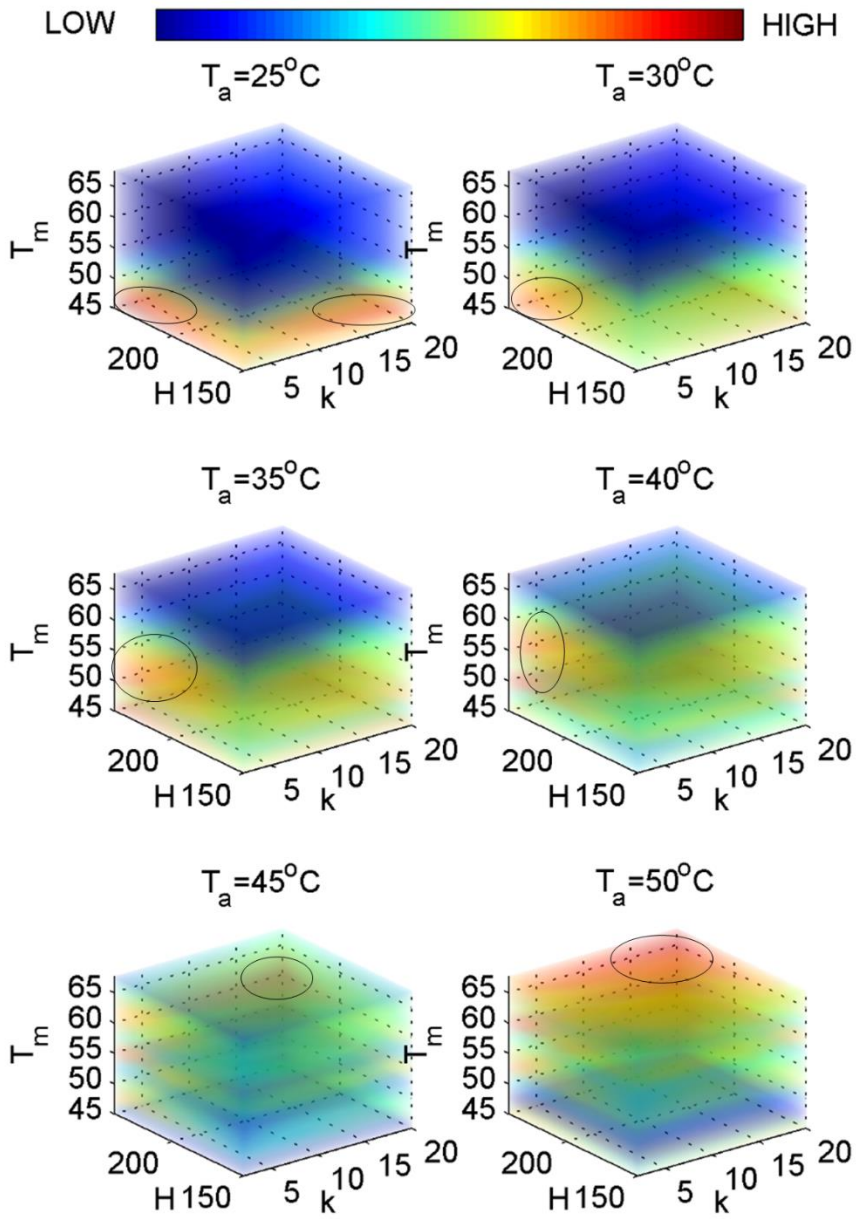

Figure 27: Maximum power for varying combination of PCM properties, at different ambient temperatures (T_a)

5.2 Case study – CPV-PCM system in Qatar

5.2.1 Weather and irradiance data

In another case study, the developed model was used to analyze the CPV-PCM power output, using real weather conditions for Qatar for the entire year. This weather data, specifically the ambient temperature and wind speed, was obtained from the Doha International Airport (ICAO callsign: OTBD) weather station, with supplemental information obtained via Wunderground.com website.

The simulation of all 365 days of a full year was found to be computationally prohibitive; it would simply take too long to run the full simulation, so instead we opted to select two consecutive days from each month as a representative of the whole month. This was done via analyzing the median and standard deviation of temperature and wind speed for each month, then selecting days whose average fell within one standard deviation. The median and standard deviation for these two quantities are shown in Figure 28 and Figure 29. The choice of two consecutive days also allows the examination of the melting and solidification behavior of the PCM. Since it is expected that the PCM operates without excessive maintenance on a yearly basis, it is useful to verify whether the PCM has solidified during the night for a new day's operation.

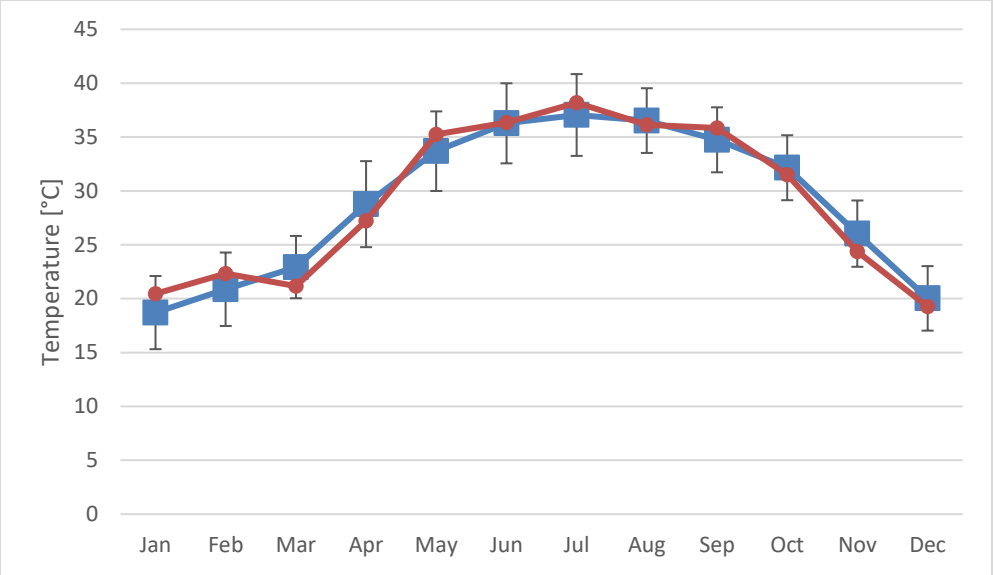

Figure 28: Average ambient temperature in Doha for the year 2015, blue line denotes average for the month, and red line is the average of the selected days

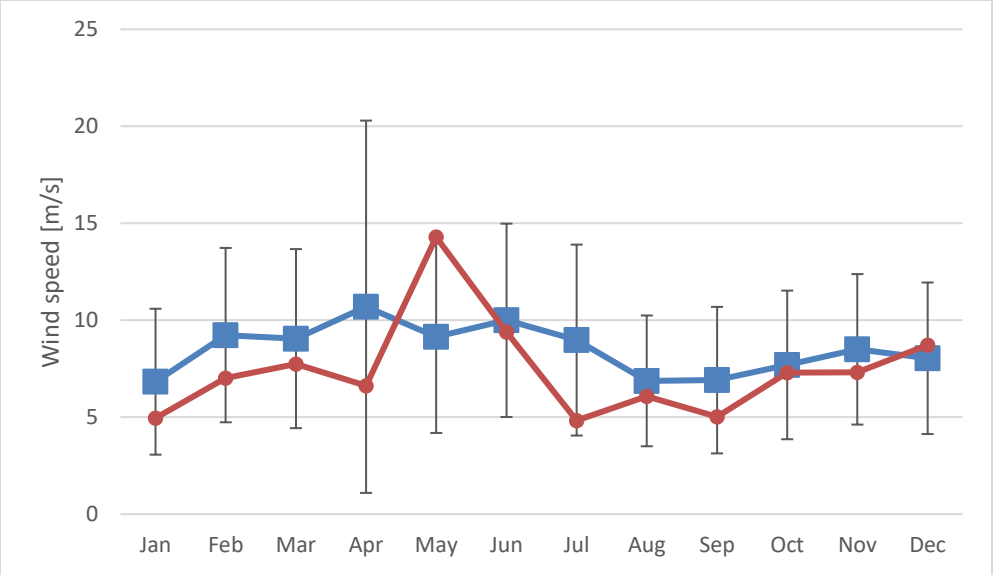

Figure 29: Average wind speed in Doha for the year 2015, blue line denotes average for the month, and red line is the average of the selected days

For the irradiance data, we used the Bird clear sky model (Bird and Hulstrom 1981). The model uses atmospheric parameters such as aerosol depth, water vapor and ozone concentration, to predict the Direct Normal Irradiance (DNI) and Global Horizontal Irradiance (GHI) that falls upon the ground on a clear day. While this model does not consider possible cloud coverage, its simplicity and accuracy allows a decent estimation of the irradiance, and ultimately the power output of the CPV system. To improve the accuracy of the results, the Bird model data was corrected to include sunrise and sunset times for the days in study, by adjusting the irradiance to be zero when the sun has set or when the sun has not risen yet.

5.2.2 PV and CPV system setups

Figure 30a shows the front view of the CPV-PCM system, while Figure 30b shows the side view of the CPV-PCM system. It is noted that the system length, which is noted as X in the figure, varies depending on the concentration ratio. The setup of the system is such that the cell width is fixed at 15 mm, and the cell length, X, is varied to provide a fair comparison based on system footprint. In this study, the CPV-PCM system will be compared with a flat-plate PV system which uses the same PV cell, adjusted by its length such that both systems occupy a $1m^2$ footprint. The cell length, X, is determined by the following equation (Sala and Antón 2011):

$$X = \frac{1}{0.015 * \frac{C_r}{0.8}} \tag{31}$$

where C_r is the optical concentration ratio desired. This ratio is divided by 0.8 to account for the concentrator losses, because to make the two footprints for CPV-PCM

and PV system comparable, the geometric concentration ratio is the factor of interest, which is the area of the aperture or concentrator entrance divided by the area of the receptor (CPV cell).

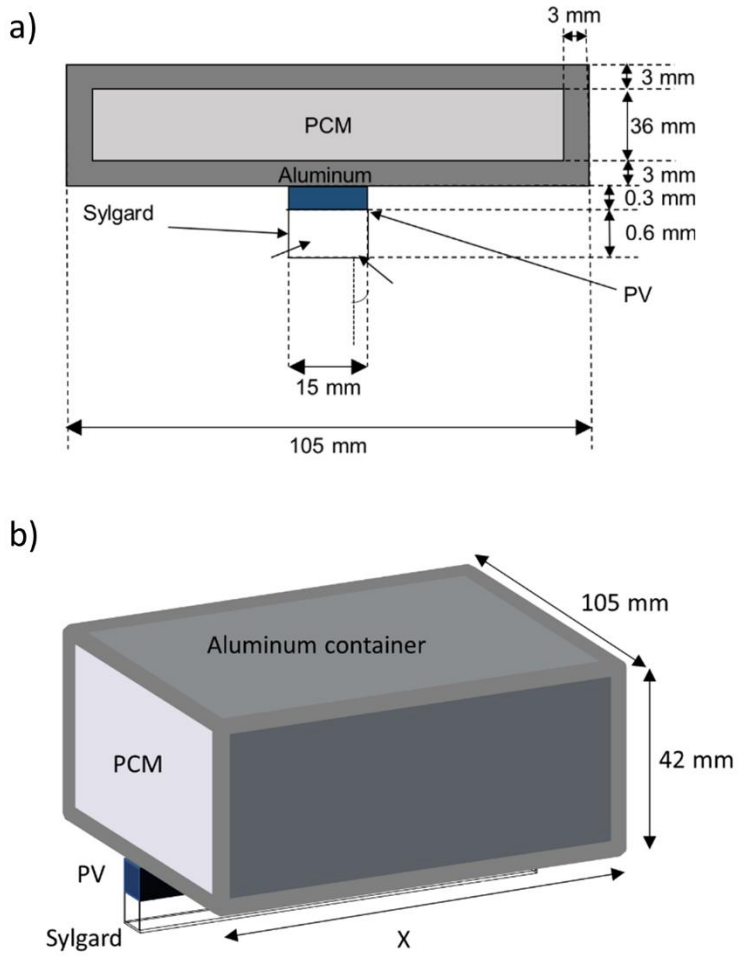

Figure 30: a) Front view of CPV-PCM system, **b)** Side view of CPV-PCM system (both not to scale)

The CPV-PCM system is assumed to have 1-axis sun tracking, i.e. the concentrator follows the movement of the sun, while the PV system is assumed to be set up at a fixed angle with no sun tracking. A schematic of the PV system is shown in Figure 31.

For the thermal model, after performing grid-time independence studies, the mesh grid for the CPV-PCM system and time step were chosen in such a way that preserves accuracy and results in shorter simulation time. For this study, a grid of 24600 elements with 75081 nodes, and a time step of 300 seconds is sufficient for these purposes.

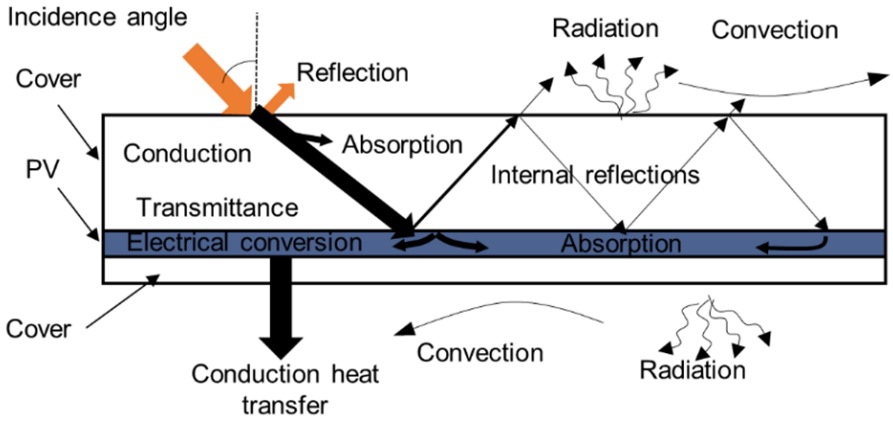

Figure 31: PV system setup

Table 3 shows a summary of the physical properties of the materials that comprise the CPV-PCM system, as well as the electrical properties of the PV cell that is used in this study. In the table, ρ is density, k is conductivity, c is the specific heat

capacity, ε is the emmisivity, H is the heat of fusion, T_m is the melting point, n is the refractive index, K is the extinction coefficient, and x is the depth of the material.

Table 3: Thermal-Optical-Electrical parameters used in Section 5.2 only

Thermal properties of system materials (Sharma, Tahir et al. 2016) (Rubitherm 2016)						
	ρ (kg m^{-3})	k (Wm^{-1}K^{-1})	c (kJ kg^{-1}K^{-1})	ε	H (kJ kg^{-1})	T_m (K)
Sylgard	1030	0.27	1.3	0.9	×	×
PV	2329	149	0.8	0.9	×	×
Aluminum	2700	205.0	0.9	×	×	×
PCM (Rubitherm RT 54HC)	850	0.2	2	×	200	326-327

Electrical properties of PV cell (Kyocera)					
I_{sc} (A)	V_{oc} (V)	I_{mp} (A)	V_{mp} (V)	K_I (%/K)	K_V (%/K)
0.794	6.09	0.736	4.87	0.0387	-0.373

Optical properties of system materials (Sarwar, Norton et al. 2016)			
	n	K (m^{-1})	x (m)
Air	1	×	×
Sylgard	1.52	4.41	0.0006
PV	4	4710	0.0003

5.2.3 PV and CPV system comparison

Using the weather and irradiance data as described in Section 5.2.1, a simulation of both the CPV-PCM and PV system operation is carried out for the full 2 days for each month of the year. The output of the three models (electrical, thermal, optical) includes the maximum power generated by the system, and the PV cell temperature.

The CPV-PCM system is simulated for optical concentration ratio of 25x, 20x and 15x. As mentioned before in Section 5.2.2, the cell length is increased whenever the concentration level is reduced, to maintain a fair comparison based on land footprint.

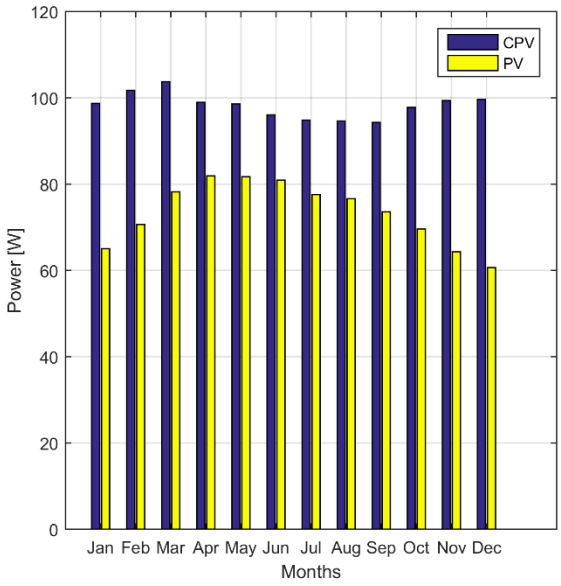

Figure 32: Maximum power for CPV-PCM and PV system at 25x optical concentration ratio

Figure 32 to Figure 34 show the maximum power produced by the CPV systems at 25x, 20x and 15x concentration, and the equivalent PV system. The maximum power for the 25x CPV on average increased by 35% over the PV system, and an increase of

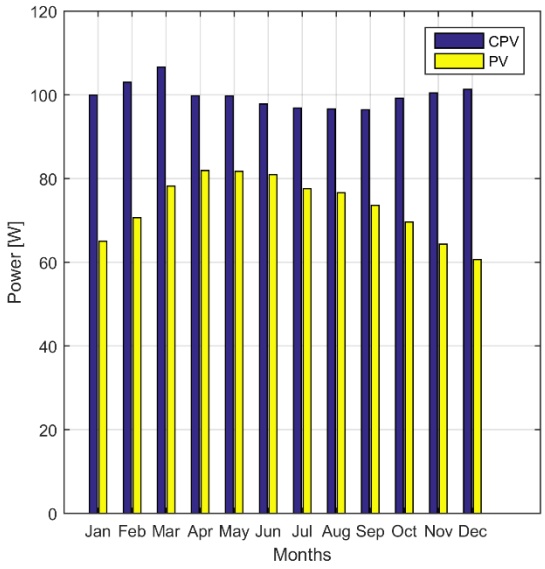

Figure 33: Maximum power for CPV-PCM and PV system at 20x optical concentration ratio

37% for the 20x CPV system over PV, plus an increase of 39% is noted for the 15x CPV system. This can be attributed to the use of tracking in the CPV system, the temperature reduction by the PCM and the increase in cell efficiency due to concentration.

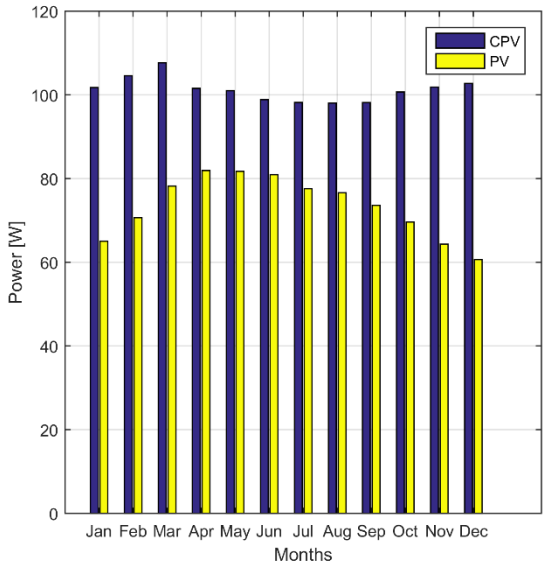

Figure 34: Maximum power for CPV-PCM and PV system at 15x optical concentration ratio

Figure 36 to Figure 38 show the electrical energy generated per day for the 25x, 20x and 15x CPV as well as the PV system. We note a large increase in energy generated, with an average increase of 95% for 25x CPV, 97% for 20x CPV, and 98% for 15x CPV over PV for the year. Compared to maximum power, energy generation sees a much larger increase. While the reasons for this increase are the same (solar tracking, cooling by PCM, increase in efficiency through concentration), solar tracking accounts for a larger contribution, since the PV only system, with its fixed inclination, misses out on important energy gains during the early and late hours of day, as shown in the comparison between tracked and untracked PV system in Figure 35.

In another point of interest, it can be noticed that the peak maximum power for the year does not coincide with the peak electrical energy for the year, for example the peak maximum power can be obtained in March, while the peak energy is obtained in May. The reason for that is simply due to the amount of sunshine hours that varies for each month, where in March, the sun only shines for 8 hours, while in May, the sun shines for 10.6 hours (QMD 2017), so naturally the energy production is higher when there is more sunshine.

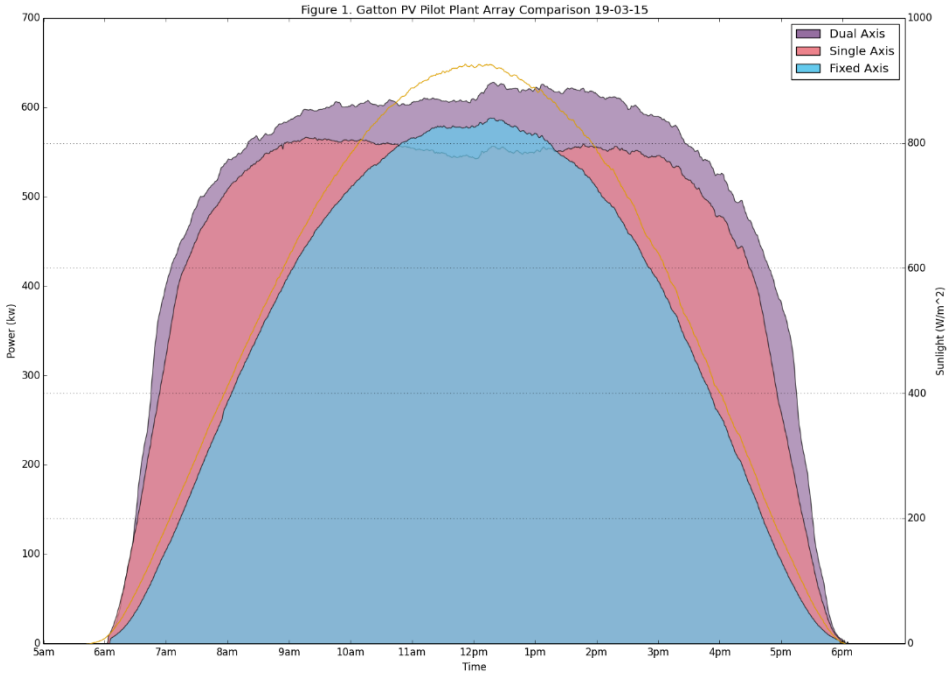

Figure 35: Irradiance profile for a PV system with single and dual axis tracking, vs a fixed axis system, reprinted from (Queensland 2017).

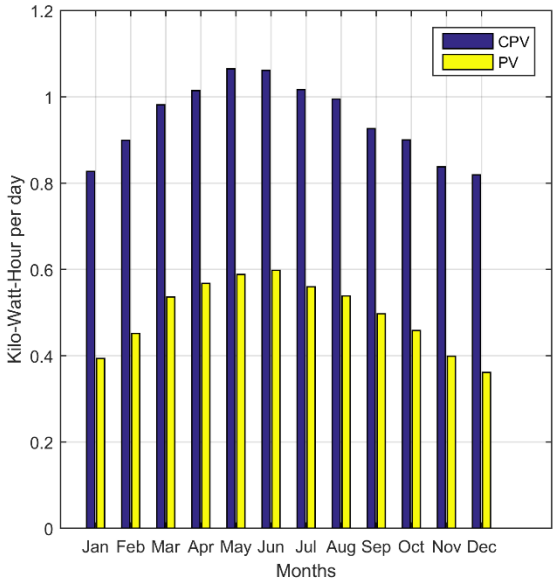

Figure 36: Electrical energy produced per day by CPV-PCM and PV system at 25x optical concentration ratio

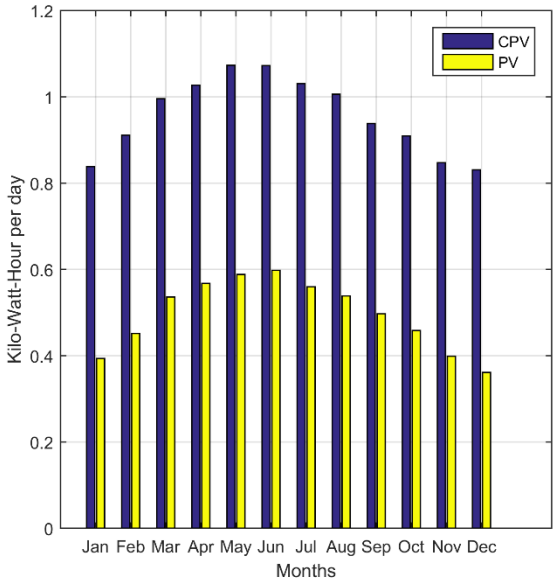

Figure 37: Electrical energy produced per day by CPV-PCM and PV system at 20x optical concentration ratio

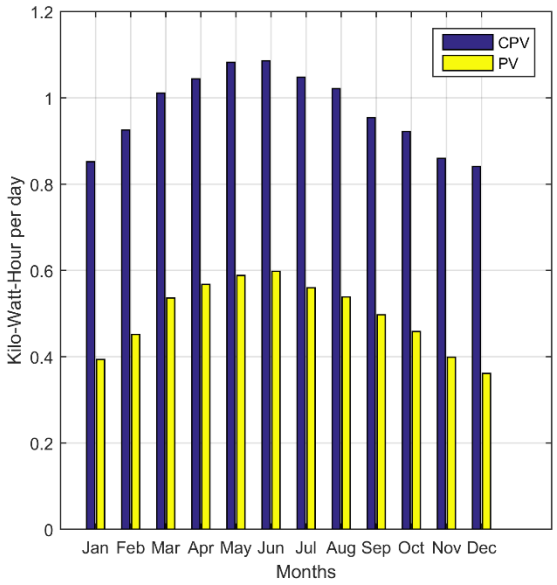

Figure 38: Electrical energy produced per day by CPV-PCM and PV system at 15x optical concentration ratio

Figure 39 to Figure 41 show the average cell temperatures for the 25x, 20x and 15x CPV system, as well as the PV system. The temperatures that were averaged are for daytime only, because power cannot be generated by the solar cell during the night, therefore the temperature during the night is largely irrelevant for this discussion. Due to the concentrating effect, the average cell temperature is higher in the CPV system over the PV system, with an average increase of 15.4 °C for 25x CPV, 9.5 °C for 20x CPV, and 2.6 °C for 15x CPV.

Even though the PCM is supposed to act as a cooling system, at the concentration levels of 15x and above, the capacity of the system is simply not enough to lower the cell temperature below the PV system's cell temperature. The PCM's main mechanism of heat absorption is through phase change, but once the melting is complete, then the

PCM acts as a sensible heat storage and can no longer maintain cell temperatures near its melting point as it is supposed to.

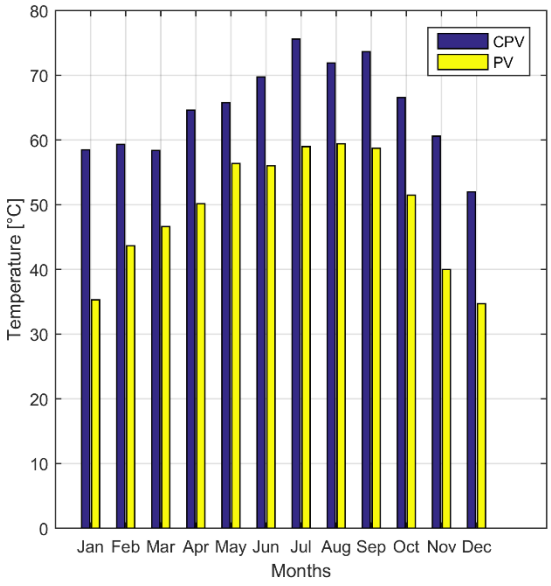

Figure 39: Average cell day temperature for CPV-PCM and PV system at 25x optical concentration ratio

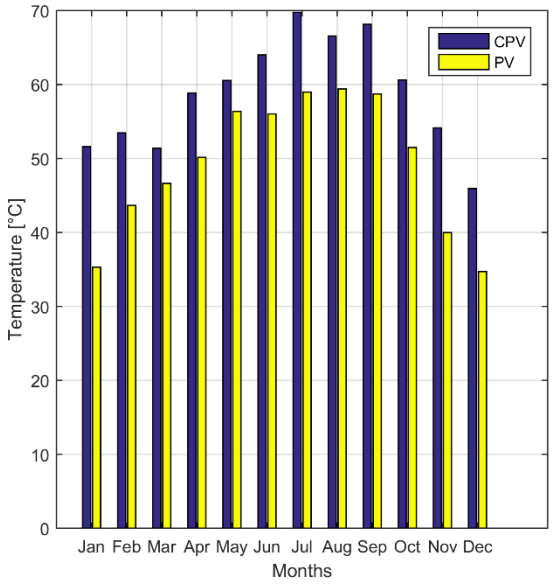

Figure 40: Average cell day temperature for CPV-PCM and PV system at 20x optical concentration ratio

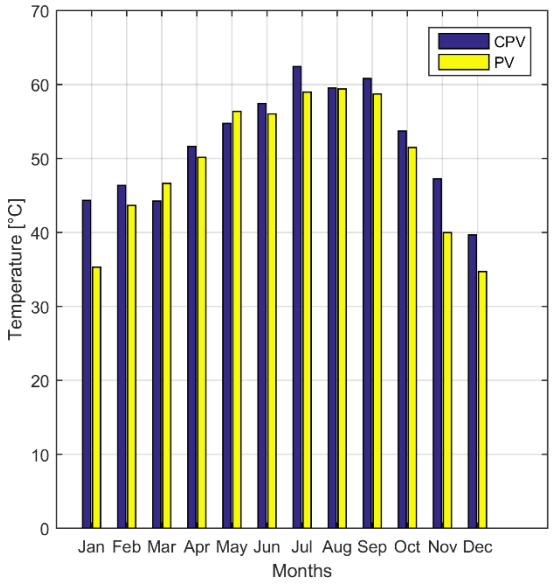

Figure 41: Average cell day temperature for CPV-PCM and PV system at 15x optical concentration ratio

In the case of 15x CPV system, the results for day temperature are more interesting, because in some months of the year the CPV system achieves a lower temperature than the PV system, unlike the 25x and 20x CPV. For example, in the month of May, the CPV system average temperature is 54.7 °C versus 56.3 °C for the PV, while in July, the CPV system average temperature is 62.4 °C versus 58.9 °C for the PV.

Because we are comparing the systems based on footprint, it is expected that for lower concentration levels, the cell sizes are longer and the PCM containers are larger. This in turns leads to a greater heat capacity potential, where the PCM can finally cool the CPV system below the PV system temperature, and in this case, 15x concentration ratio represents the threshold where this switch between high CPV/low PV and low CPV/high PV temperatures happens.

A summary of the comparison results can be seen in Table 4.

Table 4: Summary of major results of comparison of CPV-PCM system versus PV system

	Concentration Ratio		
CPV-PCM increase over PV	25x	20x	15x
Maximum power	+35%	+37%	+39%
Electrical energy per day	+95%	+97%	+98%
Average Day Temperature	+15.4 °C	+9.5 °C	+2.6 °C

6. CONCLUSION AND FUTURE WORK

6.1 Conclusion

This thesis has been primarily concerned with the development and modification of an electrical model, namely the five-parameter model, to predict the power output of a concentrator photovoltaic system. A previously developed thermal-optical model was used in conjunction with the electrical model to simulate a concentrator photovoltaic system that uses phase change materials for cooling.

The electrical model was validated against manufacturer datasheets for regular PV modules, as well as experimental results for a CPV cell, and was found in good agreement with both sets of data, where mean absolute errors were below 6.42%.

Two case studies were made with the models. The first case study investigated the effect of changing PCM properties on power output for a CPV-PCM system at two to four suns concentration level, operating for four hours, where it was found that the selection of the optimal PCM properties could yield up to 13% gain in electrical output.

The second case study investigated the yearly theoretical operation of a CPV-PCM system stationed in Qatar, at concentration levels of 15, 20 and 25 suns, versus a PV system also stationed at the same location, with both systems occupying the same footprint. The study was done using real weather data and simulated irradiance data from the Bird clear sky model. The CPV-PCM system outperformed the PV system on power generation at all concentration levels in the range (15x-25x), however the PCM was not

sufficient to cool the CPV system below the PV system temperatures, although it is expected that the lower temperatures are achieved below 15 suns concentration.

6.2 Future work

The current model offers many avenues for future development, not only for model improvement, but also in types of analysis that can be done. For the case study on Qatar, further analysis can be done on optimizing PCM properties for the 15 to 25 suns range. Although the optimal PCM would of course yield the maximum power over the year, the analysis could be coupled with data on electricity consumption patterns to select the PCM that yields the maximum power at the months of year where electricity is needed most.

Improvements could also be done for the quality of irradiance data, since clear sky models do not account for cloudy days, real irradiance data would be more valuable in making accurate predictions of solar electricity generation.

To assess the economic viability of the proposed CPV-PCM system, a cost-analysis study is important, as ultimately, the goal of CPV is to reduce the cost of solar electricity generation.

Finally, the lack of experimental data for LCPV systems does mean that the model proposed in this thesis could not be verified for the operating conditions simulated in the Qatar case study, hence, experimental data, whether indoor or outdoor, would be immensely valuable in the complete verification of the proposed model.

REFERENCES

Almonacid, F., E. Fernández, et al. (2015). "High concentrator photovoltaic module simulation by neuronal networks using spectrally corrected direct normal irradiance and cell temperature." Energy **84**(Supplement C): 336-343.

Almonacid, F., P. Rodrigo, et al. (2016). "Determination of the current–voltage characteristics of concentrator systems by using different adapted conventional techniques." Energy **101**(Supplement C): 146-160.

Amanlou, Y., T. T. Hashjin, et al. (2016). "A comprehensive review of Uniform Solar Illumination at Low Concentration Photovoltaic (LCPV) Systems." Renewable and Sustainable Energy Reviews **60**: 1430-1441.

Bird, R. E., and R. L. Hulstrom (1981). "A Simplified Clear Sky Model for Direct and Diffuse Insolation on Horizontal Surfaces.", Technical Report No. SERI/TR-642-761, Golden, CO, Solar Energy Research Institute.

Browne, M. C., B. Norton, et al. (2015). "Phase change materials for photovoltaic thermal management." Renewable and Sustainable Energy Reviews **47**: 762-782.

Ciulla, G., V. Lo Brano, et al. (2014). "A comparison of different one-diode models for the representation of I–V characteristic of a PV cell." Renewable and Sustainable Energy Reviews **32**: 684-696.

Femia, N. (2013). Power electronics and control techniques for maximum energy harvesting in photovoltaic systems. Boca Raton, Florida; London:, CRC Press, Taylor & Francis Group.

Fernández, E. F., D. L. Talavera, et al. (2016). "Investigating the impact of weather variables on the energy yield and cost of energy of grid-connected solar concentrator systems." Energy **106**: 790-801.

Friedman, D. J., J. M. Olson, et al. (2011). High-Efficiency III–V Multijunction Solar Cells. Handbook of Photovoltaic Science and Engineering, John Wiley & Sons, Ltd**:** 314-364.

Gray, J. L. (2011). The Physics of the Solar Cell. Handbook of Photovoltaic Science and Engineering, John Wiley & Sons, Ltd**:** 82-129.

Hasan, A., J. Sarwar, et al. (2017). "Yearly energy performance of a photovoltaic-phase change material (PV-PCM) system in hot climate." Solar Energy **146**: 417-429.

Hecht, E. (2002). Optics, Addison-Wesley.

Hoang, P., V. Bourdin, et al. (2014). "Coupling optical and thermal models to accurately predict PV panel electricity production." Solar Energy Materials and Solar Cells **125**: 325-338.

Humada, A. M., M. Hojabri, et al. (2016). "Solar cell parameters extraction based on single and double-diode models: A review." Renewable and Sustainable Energy Reviews **56**(Supplement C): 494-509.

Hyundai, H. I. (2014). "Hyundai Solar Module." Retrieved October, 2016, from https://shop.solardirect.com/pdf/solar-electric/modules/hyundai-perl-his-s-rg-series-datasheet-188735.pdf.

IEA. (2016). "World Energy Outlook 2016." Retrieved May 2017, from http://www.iea.org/newsroom/news/2016/november/world-energy-outlook-2016.html.

IRENA. (2016). "Renewable Energy Statistics 2016." from http://www.irena.org/DocumentDownloads/Publications/IRENA_RE_Capacity_Statistics_2016.pdf.

IRENA. (2017). "Renewable Capacity Statistics 2017." from http://www.irena.org/DocumentDownloads/Publications/RE_stats_highlights_2017.pdf.

Ishaque, K., Z. Salam, et al. (2011). "Simple, fast and accurate two-diode model for photovoltaic modules." Solar Energy Materials and Solar Cells **95**(2): 586-594.

Jakhar, S., M. S. Soni, et al. (2016). "Historical and recent development of concentrating photovoltaic cooling technologies." Renewable and Sustainable Energy Reviews **60**: 41-59.

Jawad Sarwar, A. E. A., Konstantinos E. Kakosimos (2017). Effect of the thermophysical properties of a phase change material on the electrical output of a concentrated photovoltaic system. 44th IEEE Photovoltaic Specialist Conference. Washington DC, USA, IEEE.

Khan, F., S.-H. Baek, et al. (2014). "Intensity dependency of photovoltaic cell parameters under high illumination conditions: An analysis." Applied Energy **133**(Supplement C): 356-362.

Kyocera. "KC175GHT-2 Module datasheet." 2017, from http://feyelektronik.de/downloads/Datenblaetter/Kyocera/KC175GHT-2.pdf.

Kyocera. "KC200GT Module Datasheet." 2017, from http://www.kyocera.com.sg/products/solar/pdf/kc200gt.pdf.

Lamberg, P., R. Lehtiniemi, et al. (2004). "Numerical and experimental investigation of melting and freezing processes in phase change material storage." International Journal of Thermal Sciences **43**(3): 277-287.

Lo Brano, V., A. Orioli, et al. (2010). "An improved five-parameter model for photovoltaic modules." Solar Energy Materials and Solar Cells **94**(8): 1358-1370.

Luque, A. and V. M. Andreev (2007). Concentrator photovoltaics, Berlin : Springer, [2007].

Maike Wiesenfarth, S. P. P., Andreas W. Bett, Kelsey Horowitz, Sarah Kurtz (2017) "Current Status of Concentrator Photovoltaic (CPV) Technology.", Technical Report No. TP-6A20-63916, Fraunhofer ISE, NREL.

Micheli, L., E. F. Fernández, et al. (2016). "Performance, limits and economic perspectives for passive cooling of High Concentrator Photovoltaics." Solar Energy Materials and Solar Cells **153**: 164-178.

Nelson, J. (2003). The Physics of Solar Cells, Imperial College Press.

NREL. (2017). "Best Research-Cell Efficiencies." Retrieved May 2017, from https://www.nrel.gov/pv/assets/images/efficiency-chart.png.

Peharz, G., J. P. Ferrer Rodríguez, et al. (2011). "Investigations on the temperature dependence of CPV modules equipped with triple-junction solar cells." Progress in Photovoltaics: Research and Applications **19**(1): 54-60.

Priyanka, M. Lal, et al. (2007). "A new method of determination of series and shunt resistances of silicon solar cells." Solar Energy Materials and Solar Cells **91**(2): 137-142.

QMD. (2017). "Climate Information for Doha." from http://www.qweather.gov.qa/ClimateInfo.aspx.

Queensland, U. o. (2017). "Single Axis Tracking Array." 2017, from https://www.uq.edu.au/solarenergy/pv-array/content/single-axis-tracking-array.

Quintessa. (2017). "Graph Grabber 2.0." 2017, from https://www.quintessa.org/software/downloads-and-demos/graph-grabber-2.0.

Richards, B. S. and M. A. Green (2006). Photovoltaic Cells. Wiley Encyclopedia of Biomedical Engineering, John Wiley & Sons, Inc.

Rubitherm. (2016, 31-05-2016). "RT54HC Datasheet." 2017, from https://www.rubitherm.eu/media/products/datasheets/Techdata_-RT54HC_EN_31052016.PDF.

Sala, G. and I. Antón (2011). Photovoltaic Concentrators. Handbook of Photovoltaic Science and Engineering, John Wiley & Sons, Ltd**:** 402-451.

Sarwar, J., B. Norton, et al. (2016). Effect of the phase change material's melting point on the thermal behaviour of a concentrated photovoltaic system in a tropical dry climate. EuroSun 2016, Palma de Mallorca, International Solar Energy Society.

Shanks, K., S. Senthilarasu, et al. (2016). "Optics for concentrating photovoltaics: Trends, limits and opportunities for materials and design." Renewable and Sustainable Energy Reviews **60**: 394-407.

Sharma, S., A. Tahir, et al. (2016). "Performance enhancement of a Building-Integrated Concentrating Photovoltaic system using phase change material." Solar Energy Materials and Solar Cells **149**: 29-39.

Solargis. (2017). "DNI Solar Map for Qatar." from http://solargis.com/assets/graphic/free-map/DNI/Solargis-Qatar-DNI-solar-resource-map-en.png.

Suntech. (2016). "STP275S - 20/Web Datasheet." 2017, from http://shangde.fanyacdn.com/imglibs/files/stp275s_web_(mc4_275_270_265).pdf.

Sweet, T. K. N., M. Rolley, et al. (2016). "Scalable solar thermoelectrics and photovoltaics (SUNTRAP)." AIP Conference Proceedings **1766**(1): 080007.

UN. (2014). "Energy Statistics Yearbook ", from https://unstats.un.org/unsd/energy/yearbook/default.htm.

UN. (2016). "The Paris Agreement." Retrieved May 2017, from http://unfccc.int/paris_agreement/items/9485.php.

Villalva, M. G., J. R. Gazoli, et al. (2009). "Comprehensive approach to modeling and simulation of photovoltaic arrays." IEEE Transactions on Power Electronics **24**(5): 1198-1208.

Wenham, S. R., M. A. Green, et al. (2012). Applied Photovoltaics. London, Taylor and Francis.

Zhangbo, Y., L. Qifen, et al. (2009). The cooling technology of solar cells under concentrated system. Power Electronics and Motion Control Conference, 2009. IPEMC'09. IEEE 6th International, IEEE.